Title
Parallel three-dimensional simulations of quasi-static elastoplastic solids

Authors
Boffi, Nicholas M
Rycroft, Chris H

Publication Date
2019-06-25

Peer reviewed

Parallel three-dimensional simulations of quasi-static elastoplastic solids. Part I: Numerical formulation and examples

Nicholas M. Boffi[a], Chris H. Rycroft[a,b]

[a]*Paulson School of Engineering and Applied Sciences, Harvard University, Cambridge, MA 02139*
[b]*Computational Research Division, Lawrence Berkeley Laboratory, Berkeley, CA 94720*

Abstract

In this two-part paper, we extend to three dimensions a new projection method for simulating hypo-elastoplastic solids in the quasi-static limit. The method is based on a surprising mathematical correspondence to the incompressible Navier–Stokes equations, where the projection method of Chorin (1968) is an established numerical technique. In both parts, we explore the method through numerical simulation of a three-dimensional continuum-level elastoplastic model of a bulk metallic glass based on the shear transformation zone (STZ) theory of amorphous plasticity.

Here in part I, we review the development of the quasi-static projection method, and extend it to three dimensions. We discuss the development of a three-dimensional parallel geometric multigrid solver employed to solve a linear system for the quasi-static projection. We test the method by simulating three-dimensional shear band nucleation and growth in materials undergoing simple shear, and explore the agreement of the method with an explicit timestepping method as the quasi-static limit is mathematically approached. We consider several three-dimensional examples and contrast the dynamics of shear banding in these situations with previous two-dimensional studies. We consider the generation of physically realistic randomly distributed initial conditions in a relevant STZ internal variable, and discuss relevance to experimental studies of shear banding.

Keywords: fluid mechanics, Chorin-type projection method, plasticity, elastoplasticity

1. Introduction

Elastoplastic behavior is ubiquitous in materials of modern engineering relevance and scientific inquiry, including metal matrix composites [1], auxetics [2], granular materials [3], and amorphous materials such as gels [4], thin films [5], and bulk metallic glasses (BMGs) [6]. Elastoplastic behavior is defined as any combination of elastic and plastic deformation, and admits a number of mathematical descriptions [7]. For stress levels below the material yield stress, the material deforms purely elastically and returns to its undeformed state upon

Email addresses: boffi@g.harvard.edu (Nicholas M. Boffi), chr@seas.harvard.edu (Chris H. Rycroft)

removal of the load. When the yield stress is reached, the material begins to deform plastically, leading to permanent, irreversible deformation that persists beyond load removal [8].

The mathematical representation of elastoplasticity is fundamental to its study, and any modeling choice amounts to a description of the interaction of the elastic and plastic components of deformation at a microscopic level [9]. An in-depth understanding of the limitations of each formulation is a target of modern research, and the development of an optimal theoretical framework has remained elusive [7]. Two of the most popular choices are hyper-elastoplasticity [10, 11] and hypo-elastoplasticity [12]. In hyper-elastoplasticity, the deformation gradient is decomposed *multiplicatively* into the product of an elastic part and a plastic part, $\mathbf{F} = \mathbf{F}_e\mathbf{F}_p$. In hypo-elastoplasticity, the Eulerian rate of deformation tensor is decomposed *additively* into elastic and plastic parts, $\mathbf{D} = \mathbf{D}^{\text{el}} + \mathbf{D}^{\text{pl}}$ [13]. Hypo-elastoplasticity has some drawbacks, but is well-suited to problems with small elastic deformation and large plastic deformation. We focus on hypo-elastoplasticity in the remainder of this article.

The hypo-elastoplastic formulation has several numerical advantages. Since it is based on the Eulerian rate of deformation tensor, it is well-suited to a fixed-grid framework. Fixed grids have simpler topologies than their Lagrangian counterparts, and are easier to program and to parallelize. This is particularly important in three dimensions, where the computational expense mandates parallelization techniques, and the implementation difficulty increases. Fixed-grid methods are the methods of choice for fluid simulation [14, 15, 16] and are useful for fluid–structure interaction [17, 18, 19]. Fixed-grid frameworks allow a wider range of numerical linear algebra techniques to be used, such as the geometric multigrid method [20, 21].

The additive decomposition of $\mathbf{D}$, coupled with the linear-elastic constitutive relation and a continuum formulation of Newton's second law, leads to a closed system of partial differential equations for the material velocity, stress, and internal variables intrinsic to the plasticity model. These equations can be solved via an explicit finite-difference discretization scheme. Such explicit methods resolve elastic waves, and their timesteps are restricted by the well-known Courant–Friedrichs–Lewy (CFL) condition [22]. The CFL condition states that $\Delta t \leq \frac{h}{c_e}$ is necessary for numerical stability, where c_e is a typical elastic wave speed in the medium and h is the grid spacing. In metals and other materials of interest, elastic waves can travel at kilometers per second. The CFL condition thus poses a prohibitive limit on the timestep, and the development of alternative simulation approaches is necessary.

After scaling the hypo-elastoplastic equations to the long time and small velocity limit, the continuum version of Newton's second law can be replaced by a constraint that the stresses must remain in quasi-static equilibrium [23]. This leads to an explicit update equation for the stress tensor, still given by linear elasticity and dependent on the velocity, coupled with a quasi-static constraint on the stress tensor. In this limit, there is a surprising mathematical analogy with incompressible fluid flow. The incompressible limit of the Navier–Stokes equations replaces an explicit equation for the fluid pressure with a divergence-free constraint on the fluid velocity, but the explicit equation for the velocity is unaffected. A well-known algorithm for this setting is the projection method of Chorin [24, 25]. In this method, the velocity field is first updated explicitly, but this intermediate velocity does not obey the incompressibility constraint. An elliptic problem is solved which simultaneously enforces the

incompressibility constraint and enables computation of the pressure. A similar algorithm was recently developed for the quasi-static limit of hypo-elastoplasticity and studied in two dimensions [23]. The stress is first updated explicitly such that the intermediate value does not obey the quasi-static constraint. The stress tensor is then projected back onto the manifold of divergence-free solutions through an elliptic problem for the velocity. Importantly, this quasi-static projection method does not resolve elastic waves, and hence enables timesteps that are orders of magnitude larger than those required by the CFL condition. In this work, we extend the quasi-static projection algorithm to three dimensions, and place it on a firmer theoretical footing by making a connection to more general projection methods in fluid dynamics.

As a physical testbed for our methodology, we employ an athermal formulation of the STZ theory of Falk, Langer, Bouchbinder and coworkers as a plasticity model for a bulk metallic glass [26, 27, 28, 29]. The combination of the STZ theory and BMG modeling is an excellent setting for our three-dimensional method. Metallic glasses naturally lend themselves to study through the hypo-elastoplasticity framework, as their elastic deformation is generally small and well-described by a linear theory, yet they can exhibit significant plastic deformation [30]. Their elastic moduli are typically on the order of 10–100 GPa, and hence experimental loading conditions often place samples in the quasi-static regime [31]. They present interesting and poorly understood fundamental physics [32, 33, 34, 35]. A useful test case has been to study the necking instability in a bar under uniaxial tension [36, 37, 38] since it highlights the interplay between elastic and plastic deformation. The physical mechanisms of BMG fracture were explored using the two-dimensional projection method [39, 23], subsequently allowing BMGs fracture toughness to be predicted across a wide range of experimental conditions [40]. Later experimental measurements due to Ketkaew *et. al.* demonstrated that these simulation-based predictions were quantitatively correct [41]. Indeed, testable predictions for complex amorphous systems such as BMGs are rare, and the development of efficient numerical methods such as the ones presented here provide a way to generate them, and to guide future experimental inquiry.

Under loading, BMGs exhibit shear bands [42], a nonlinear instability characterized by rapid strain localization [43] along a thin band [44] within the material. Experimentally, shear bands rapidly lead to material failure [45, 46], and are one of the primary limitations in employing BMGs in applications [47]. Analytical work probing shear bands in amorphous materials is difficult, particularly in two or three dimensions, which highlights a need for computational investigations. The development of our method enables the study of shear-banding in three dimensions at large scale and high resolution without excessive computational expense. Our simulations demonstrate that this scale and resolution is indeed necessary, and expose interesting fine-scale and uniquely three-dimensional features of shear banding. Our methodology opens the door to future studies probing the shape, structure, and topology of shear bands, as well as the mechanism and statistical properties of their formation.

We emphasize that though the STZ theory is a useful test case for our method both physically and numerically, the algorithm is general and can be used for many plasticity models within the hypo-elastoplasticity framework. This could include free-volume based

models of BMGs [48], hypo-elastic materials [49, 50, 51], geophysical models [52, 53], and rate-independent plasticity models [54, 55, 56, 57]. We also emphasize that Chorin's projection method represents a first step towards more complex projection-based algorithms such as gauge methods [58, 59, 60] and pressure-Poisson methods [61, 62], and that we have laid the groundwork here to generalize these algorithms to the case of hypo-elastoplasticity.

The structure of this paper is as follows. In Section 2, we formally describe the relation between Chorin's projection method and the projection algorithm for hypo-elastoplasticity employed here. In Section 3, we describe a finite-difference implementation of our projection method, and describe a forward-Euler based explicit method for solving the hypo-elastoplastic equations in the non-quasi-static limit. We also discuss our development of a parallel geometric multigrid method used for the stress projection. In Section 4, we demonstrate convergence between the explicit and projection methods in a regime in which the two are expected to produce similar results, and study several interesting examples of shear banding dynamics in a metallic glass. We conclude with some interim remarks in Sec. 5, and our work is continued in part II [63], where the projection method is extended to an arbitrary reference domain via a domain transformation.

2. Projection methods for fluid dynamics and hypo-elastoplasticity

2.1. Hypo-elastoplasticity

We denote by $\boldsymbol{\sigma}(\mathbf{x},t)$ the Cauchy stress tensor and by $\mathbf{v}(\mathbf{x},t)$ the velocity field at a position $\mathbf{x}$ and time t in a material. The total rate of deformation tensor $\mathbf{D}$ is defined as the symmetric part of the velocity gradient, $\mathbf{D} = \frac{1}{2}(\nabla\mathbf{v} + (\nabla\mathbf{v})^{\mathsf{T}})$. For any field $f(\mathbf{x},t)$, we define the advective time derivative by $\frac{df}{dt} = \frac{\partial f}{\partial t} + (\mathbf{v}\cdot\nabla)f$. The fundamental assumption of hypo-elastoplasticity is that the rate of deformation tensor can be additively decomposed into a sum of elastic and plastic parts, $\mathbf{D} = \mathbf{D}^{\mathrm{el}} + \mathbf{D}^{\mathrm{pl}}$.

For stiff elastoplastic materials with small elastic deformation, the linear elastic constitutive law provides an accurate description,

$$\frac{\mathcal{D}\boldsymbol{\sigma}}{\mathcal{D}t} = \mathbf{C} : \mathbf{D}^{\mathrm{el}} = \mathbf{C} : \left(\mathbf{D} - \mathbf{D}^{\mathrm{pl}}\right). \tag{1}$$

$\mathbf{C}$ is the fourth-rank stiffness tensor, taken to be homogeneous and isotropic. With Lamé's first parameter λ and shear modulus μ, the components of $\mathbf{C}$ are given by $C_{ijkl} = \lambda\delta_{ij}\delta_{kl} + \mu\left(\delta_{ik}\delta_{jl} + \delta_{il}\delta_{jk}\right)$ [64]. The time derivative $\frac{\mathcal{D}\boldsymbol{\sigma}}{\mathcal{D}t} = \frac{d\boldsymbol{\sigma}}{dt} - \mathbf{L}^{\mathsf{T}}\boldsymbol{\sigma} - \boldsymbol{\sigma}\mathbf{L} + \mathrm{Tr}(L)\boldsymbol{\sigma}$ denotes the Truesdell objective stress rate, where $\mathbf{L}$ is the velocity gradient $\mathbf{L} = \nabla\mathbf{v}$.[1]

[1]The Truesdell rate is usually presented in the form $\frac{\mathcal{D}\boldsymbol{\sigma}}{\mathcal{D}t} = \frac{d\boldsymbol{\sigma}}{dt} - \mathbf{L}\boldsymbol{\sigma} - \boldsymbol{\sigma}\mathbf{L}^{\mathsf{T}} + \mathrm{Tr}(L)\boldsymbol{\sigma}$. In this work we have replaced $\mathbf{L}^{\mathsf{T}}$ in the standard definition with $\mathbf{L}$ [8]. The standard form of the Truesdell rate defines $\mathbf{L}$ as the Fréchet derivative of the velocity field. We use the symbol $\nabla\mathbf{v}$ to denote the *gradient* of the the velocity field; formally, the gradient of a vector field is the transpose of its Fréchet derivative. The coordinate transformation methodology presented in part II of this work requires the use of both vector field gradients and Fréchet derivatives, and hence we distinguish between the two here. This corresponds to the convention $(\nabla\mathbf{f})_{ij} = \partial_i f_j$ for the gradient of a vector field (*i.e.*, the derivatives go row-wise).

From Newton's second law, the material velocity obeys the equation

$$\rho \frac{d\mathbf{v}}{dt} = \nabla \cdot \boldsymbol{\sigma} \tag{2}$$

where ρ denotes the material density. Equations 1 & 2 form a hyperbolic system of equations for the stress and velocity fields, which can be solved explicitly using standard finite-difference simulation methods. This hyperbolic system will resolve elastic waves, and so the timestep Δt and grid spacing Δx must satisfy the CFL condition $\Delta t \leq \Delta x / c_e$ for numerical stability, where c_e is an elastic wave speed. In materials such as metals and metallic glasses, elastic waves travel on the order of kilometers per second. Spatial discretizations capable of resolving fine-scale features of interesting physical phenomena in these materials can be as small as micrometers. For $\Delta x = 1$ µm and $c_e = 1$ km/s, the CFL condition requires $\Delta t \leq 1$ ns, an extreme restriction for phenomena that occur on realistic timescales.

2.2. Quasi-static hypo-elastoplasticity

We consider a scenario in which plastic deformation occurs on a timescale much greater than the time for waves to propagate through the material. In this setting, macroscopic plastic deformation takes place due to the accumulation of small velocity gradients over long times. The details of a limiting procedure describing this physical regime were performed in previous two-dimensional work [23] and will not be reproduced here.

In this quasi-static limit, the equation for the velocity in Eq. 2 can be approximately replaced by a constraint on the stress

$$\nabla \cdot \boldsymbol{\sigma} \approx \mathbf{0}. \tag{3}$$

Equation 3 is referred to as the quasi-staticity constraint. The evolution equation for the stress in Eq. 1 is unaffected by the limiting procedure, and hence Eq. 1 must be solved subject to the global constraint Eq. 3 to obtain solutions valid in this limit.

At this stage, it is unclear how to do so. The velocity $\mathbf{v}$ appears in Eq. 1 through $\mathbf{D}$, but there is no longer an equation that can be integrated explicitly to solve for it. It is also not guaranteed that solutions of Eq. 1 subject to the constraint in Eq. 3 will agree with solutions of Eq. 1 and Eq. 2.

2.3. Incompressible fluid dynamics

We now demonstrate an analogy between the computational issues presented in the previous section and those encountered in incompressible fluid dynamics. Consider a fluid with velocity $\mathbf{v}$, pressure p, and density ρ. The fluid velocity field obeys the Navier–Stokes equation,

$$\frac{d\mathbf{v}}{dt} = -\nabla p + \nu \nabla^2 \mathbf{v}. \tag{4}$$

The fluid density satisfies

$$\frac{d\rho}{dt} = -\rho \left(\nabla \cdot \mathbf{v} \right), \tag{5}$$

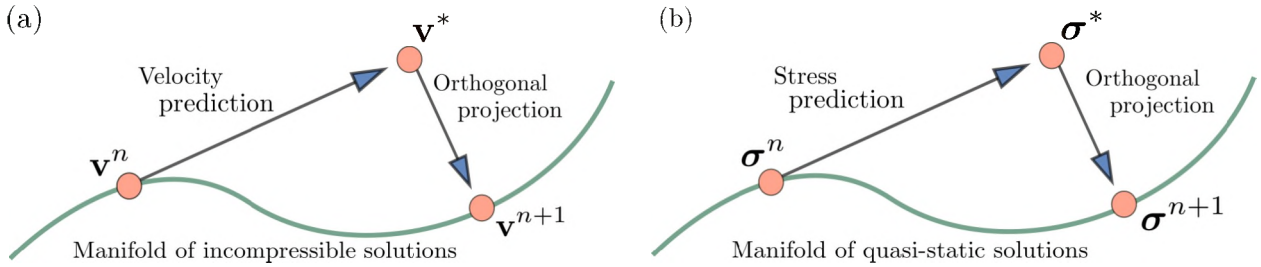

Figure 1: The projection-based timestepping scheme for (a) the velocity field in incompressible fluid dynamics and (b) the stress tensor in quasi-static hypo-elastoplasticity. In both cases, an intermediate field value (denoted with a superscript $*$) is first computed which does not obey the divergence-free constraint. This intermediate field value is then projected back onto the manifold of divergence-free solutions to compute the field at the next timestep.

along with an equation of state linking the fluid density to the fluid pressure. Using an explicit scheme to solve the hyperbolic system in Eqs. 4 & 5 will resolve sound waves in the fluid, which leads to timestep restrictions from the CFL condition. In the long-time limit, Eq. 5 is traded for the *incompressibility constraint* on the velocity field,

$$\nabla \cdot \mathbf{v} = 0. \tag{6}$$

This limit reduces the coupled partial differential equations for the pressure and velocity to a single constrained equation for the velocity. The pressure is present in the equation for the velocity, though its evolution equation has been exchanged for the incompressibility constraint; this is much like the quasi-static limit of hypo-elastoplasticity described in the preceding section.

Chorin [24, 25] developed a numerical method for this system of equations that involves the use of an orthogonal projection, spurring significant research into related algorithms [61, 62]. Such projection methods proceed via a two-step procedure, where an intermediate velocity $\mathbf{v}^*$ is first computed which does not obey the incompressibility constraint. $\mathbf{v}^*$ is then orthogonally projected onto the manifold of divergence-free solutions through the solution of an elliptic problem for an auxiliary field related to the pressure. The process of projection simultaneously enforces the constraint and enables computation of the pressure field.

One typical approach is to employ a Hodge decomposition [61, 62],

$$\mathbf{v}^* = \mathbf{v} + \nabla\phi, \tag{7}$$

where $\mathbf{v}$ is the desired divergence-free velocity field and ϕ is an auxiliary field. One then updates $\mathbf{v}^*$ via the equation

$$\mathbf{v}_t^* + (\mathbf{v} \cdot \nabla)\,\mathbf{v} + \nabla q = \nu\nabla^2\mathbf{v}^*, \tag{8}$$

where ∇q is an approximation to the pressure gradient. Substituting Eq. 7 into Eq. 8 leads to a formula for the pressure

$$\nabla p = \nabla\,(q + \phi_t) - \nu\nabla^2\nabla\phi, \tag{9}$$

from which p can be computed. The divergence of Eq. 7 implies that $\nabla \cdot \mathbf{v} = 0$ if ϕ is such that

$$\nabla^2 \phi = \nabla \cdot \mathbf{v}^*. \tag{10}$$

The Poisson problem in Eq. 10 can be solved for ϕ using standard techniques of numerical linear algebra, and the projection can be completed by computing $\mathbf{v} = \mathbf{v}^* - \nabla\phi$. Boundary conditions on ϕ depend on the physical scenario of interest, and are critical for obtaining higher-order methods [61, 62]. The algorithm proceeds by setting $\mathbf{v}^* = \mathbf{v}$. This procedure is schematically represented in discrete-time in Fig. 1(a). Projection methods avoid the CFL condition associated with compressive waves in the fluid, and hence can use significantly larger timesteps than explicit methods.

It is possible to demonstrate that solving Eq. 10 represents an orthogonal projection. We define the inner product between two vector-valued fields,

$$\langle \mathbf{v}, \mathbf{u} \rangle = \int_\Omega \mathbf{v} \cdot \mathbf{u} \, d^3\mathbf{x}, \tag{11}$$

where Ω is the simulation domain. Using this inner product, we can compute

$$\begin{aligned} \langle \mathbf{v}^{n+1} - \mathbf{v}^n, \mathbf{v}^{n+1} - \mathbf{v}^* \rangle &= -\int_\Omega \left(\mathbf{v}^{n+1} - \mathbf{v}^n \right) \cdot \nabla\phi(\mathbf{x}) d^3\mathbf{x} \\ &= \int_\Omega \left(\nabla \cdot \mathbf{v}^{n+1} - \nabla \cdot \mathbf{v}^n \right) \phi(\mathbf{x}) d^3\mathbf{x} = 0, \end{aligned} \tag{12}$$

thereby establishing that the projection $\mathbf{v}^{n+1} - \mathbf{v}^*$ is orthogonal to the difference between the two velocity fields, $\mathbf{v}^{n+1} - \mathbf{v}^n$.

2.4. A family of projection methods for hypo-elastoplasticity

We now formulate a three-dimensional projection method for solving Eq. 1 subject to the quasi-static constraint Eq. 3. We define an intermediate stress

$$\boldsymbol{\sigma}^* = \boldsymbol{\sigma} + \mathbf{C} : \nabla\boldsymbol{\Phi}, \tag{13}$$

where $\boldsymbol{\Phi}(\mathbf{x}, t)$ is an auxiliary vector field. We can solve for $\boldsymbol{\sigma}^*$ by dropping the $\mathbf{C} : \mathbf{D}$ term in Eq. 1,

$$\boldsymbol{\sigma}^*_t + (\mathbf{v} \cdot \nabla)\, \boldsymbol{\sigma} = \mathbf{L}^\mathsf{T}\boldsymbol{\sigma} + \boldsymbol{\sigma}\mathbf{L} - \mathrm{Tr}(\mathbf{L})\boldsymbol{\sigma} + \mathbf{C} : \left(\nabla\mathbf{q} - \mathbf{D}^{\mathrm{pl}} \right). \tag{14}$$

In Eq. 14, $\mathbf{q}$ represents an approximation to the velocity $\mathbf{v}$. Substituting Eq. 13 into Eq. 14, we find

$$\mathbf{C} : \mathbf{D} = \mathbf{C} : \nabla \left(\mathbf{q} - \boldsymbol{\Phi}_t \right), \tag{15}$$

from which $\mathbf{D}$ can be computed. Taking the divergence of Eq. 13 and requiring $\nabla \cdot \boldsymbol{\sigma} = \mathbf{0}$, $\boldsymbol{\Phi}$ must satisfy the equation

$$\nabla \cdot (\mathbf{C} : \nabla\boldsymbol{\Phi}) = \nabla \cdot \boldsymbol{\sigma}^*. \tag{16}$$

Equation 16 is a linear system with source term $\nabla \cdot \boldsymbol{\sigma}^*$ that can be solved for $\boldsymbol{\Phi}$. Once $\boldsymbol{\Phi}$ has been found, $\boldsymbol{\sigma}^*$ is projected onto the manifold of divergence-free solutions by computing

Table 1: Material parameters used in this study, for both linear elasticity and the STZ model of amorphous plasticity. The Boltzmann constant k_B is used to convert energetic values to temperatures.

Parameter	Value
Young's modulus E	101 GPa
Poisson ratio ν	0.35
Bulk modulus K	122 GPa
Shear modulus μ	37.4 GPa
Density ρ_0	6125 kg m^{-3}
Shear wave speed c_s	2.47 km s^{-1}
Yield stress s_Y	0.85 GPa
Molecular vibration timescale τ_0	10^{-13} s
Typical local strain ϵ_0	0.3
Effective heat capacity c_0	0.4
Typical activation barrier Δ/k_B	8000 K
Typical activation volume Ω	300 Å^3
Thermodynamic bath temperature T	400 K
Steady state effective temperature χ_∞	900 K
STZ formation energy e_z/k_B	21000 K

$\boldsymbol{\sigma} = \boldsymbol{\sigma}^* - \mathbf{C} : \nabla\boldsymbol{\Phi}$. The algorithm then proceeds by setting $\boldsymbol{\sigma}^* = \boldsymbol{\sigma}$, and is represented schematically in Fig. 1(b). A projection method is defined by the choice of the approximate velocity field $\mathbf{q}$, the auxiliary vector field $\boldsymbol{\Phi}$, and the integration method for Eq. 14.

As in the case of fluid dynamics, we can show that the projection is orthogonal in a suitable inner product. To do so, we define an inner product between two stress tensors as in [23],

$$\langle \boldsymbol{\sigma}, \boldsymbol{\sigma}' \rangle = \int_\Omega \boldsymbol{\sigma} : \mathbf{S} : \boldsymbol{\sigma}' \, d^3\mathbf{x}, \tag{17}$$

where $\mathbf{S} = \mathbf{C}^{-1}$ is the stiffness tensor. Equation 17 computes the elastic strain energy of a material with stress field $\boldsymbol{\sigma}$ and strain field $\mathbf{S} : \boldsymbol{\sigma}'$, or vice-versa by symmetry. Because $\mathbf{S}$ is a symmetric positive definite tensor for physically realistic Lamé parameters, this definition is an inner product. By explicit computation,

$$\begin{aligned}
\langle \boldsymbol{\sigma}^{n+1} - \boldsymbol{\sigma}^n, \boldsymbol{\sigma}^{n+1} - \boldsymbol{\sigma}^* \rangle &= \int \left(\boldsymbol{\sigma}^{n+1} - \boldsymbol{\sigma}^n\right) : \mathbf{S} : \mathbf{C} : \nabla\boldsymbol{\Phi} \, d^3\mathbf{x} \\
&= \int \left(\boldsymbol{\sigma}^{n+1} - \boldsymbol{\sigma}^n\right) : \nabla\boldsymbol{\Phi} \, d^3\mathbf{x} \\
&= -\int \left(\nabla \cdot \boldsymbol{\sigma}^{n+1} - \nabla \cdot \boldsymbol{\sigma}^n\right) \cdot \boldsymbol{\Phi} \, d^3\mathbf{x} = 0.
\end{aligned} \tag{18}$$

3. Numerical implementation

In this section, we describe an implementation of an explicit forward Euler method to solve Eqs. 1 & 2, as well as a specific instance of the quasi-static projection method in Eqs. 14

& 16. We model elastoplastic deformation in a BMG using an athermal variant of the STZ theory.

3.1. Plasticity model

As a plasticity model for a metallic glass, we use an athermal form of the STZ theory suitable for studying diverse materials including BMGs below the glass transition temperature, dense granular materials, and soft materials such as foams or colloidal glasses [27, 28]. Within the STZ theory, irreversible molecular rearrangements are assumed to occur sporadically throughout an otherwise elastic material, and each rearrangement induces a small increment of strain. The accumulation of many such events leads to macroscopic plastic deformation. These rearrangements are assumed to occur at rare, localized, sites known as STZs when local stresses surpass the material yield stress s_y. Thermal fluctuations of the atomic configuration are neglected in the athermal formulation: molecular rearrangements are entirely driven by external mechanical forces. Thermal theories introduce additional coupling between a *configurational* subsystem governing the rearrangements that occur at the STZs, and a *kinetic/vibrational* subsystem governing the thermal vibrations of atoms in their cage of nearest neighbors [65].

STZs may be conceptualized as clusters of atoms predisposed to configurational rearrangements when subjected to external shear [27]. Each rearrangement corresponds to a transition in the configurational energy landscape; these transitions are usually towards a lower-energy configuration, but there is a small probability for a reverse transition. Before the application of external shear, the material sample is at a local minimum. External shear alters the shape of the energy landscape, and can make transitions to other states considerably more likely.

The density of STZs in space follows a Boltzmann distribution in an effective disorder temperature denoted by χ [66, 67, 68, 69]. χ governs the out-of-equilibrium configurational degrees of freedom of the material and has many properties of the usual temperature: it is measured in Kelvin, and can be obtained as the derivative of a configurational energy with respect to a configurational entropy [70]. χ is distinct from the thermodynamic temperature T, though it plays the same role for the configurational subsystem as T does for the kinetic/vibrational subsystem.

The plastic rate of deformation tensor is proportional to the deviatoric part of the stress tensor $\boldsymbol{\sigma}_0 = \boldsymbol{\sigma} - \frac{1}{3}\mathbf{I}\,\mathrm{tr}(\boldsymbol{\sigma})$, so that $\mathbf{D}^{\mathrm{pl}} = D^{\mathrm{pl}}\frac{\boldsymbol{\sigma}_0}{\bar{s}}$. $\bar{s}$ is a local stress measure given by the Frobenius norm of the deviatoric stress tensor, $\bar{s}^2 = \frac{1}{2}\sum_{ij}\sigma_{0,ij}^2$. The magnitude of the plastic rate of deformation is given by

$$\tau_0 D^{\mathrm{pl}} = e^{-e_z/k_B\chi}\mathcal{C}(\bar{s},T)\left(1-\frac{s_Y}{\bar{s}}\right), \tag{19}$$

where τ_0 is a molecular vibration timescale, e_z is a typical STZ formation energy, and k_B is the Boltzmann constant. $\mathcal{C}(\bar{s},T)$ represents the total STZ transition rate. With $\mathcal{R}(\pm\bar{s},T)$ denoting the forward and reverse rates between two configurational states, the total transition rate is $\mathcal{C}(\bar{s},T) = \frac{1}{2}\left(\mathcal{R}(\bar{s},T)+\mathcal{R}(-\bar{s},T)\right)$. The transitions follow a linearly stress-biased thermal activation process,

$$\mathcal{R}(\pm\bar{s},T) = \exp\left(-\frac{\Delta \mp \Omega\epsilon_0\bar{s}}{k_B T}\right). \tag{20}$$

Δ is a typical energetic barrier for a transition, Ω is a typical STZ volume, and ϵ_0 is a typical local strain due to an STZ transition. While thermal fluctuations are neglected in the athermal model, the thermodynamic temperature still sets the magnitude of transition rates in the system. Using the form Eq. 20 yields the overall transition rate

$$\mathcal{C}(\bar{s}, T) = e^{-\Delta/k_B T} \cosh\left(\frac{\Omega \epsilon_0 \bar{s}}{k_B T}\right). \tag{21}$$

The effective temperature satisfies [27, 71, 32, 33]

$$c_0 \frac{d\chi}{dt} = \frac{\left(\mathbf{D}^{\mathrm{pl}} : \boldsymbol{\sigma}_0\right)}{s_Y} \left(\chi_\infty - \chi\right) + l^2 \nabla \cdot \left(D^{\mathrm{pl}} \nabla \chi\right). \tag{22}$$

Equation 22 consists of a term causing growth to an asymptotic value χ_∞ and a diffusive term with diffusion length scale l. Both saturation to χ_∞ and diffusion occur in response to plastic deformation. The term $\mathbf{D}^{\mathrm{pl}} : \boldsymbol{\sigma}_0$ is the rate of energy dissipated by externally applied mechanical work, so that STZs are created and annihilated proportional to this rate. c_0 is an effective heat capacity; Eq. 22 is thus essentially a heat equation, representing the first law of thermodynamics for the configurational subsystem [27]. The interdependence of Eqs. 19 & 22 enables the development of shear bands via positive feedback, as increasing χ also increases D^{pl} [32, 33].

3.2. Explicit method

An explicit forward Euler discretization of Eq. 2 reads

$$\rho \frac{\mathbf{v}^{n+1} - \mathbf{v}^n}{\Delta t} = -\left(\mathbf{v}^n \cdot \nabla\right) \mathbf{v}^n + \nabla \cdot \boldsymbol{\sigma}^n + \kappa \nabla^2 \mathbf{v}^n. \tag{23}$$

The small viscous stress term $\kappa \nabla^2 \mathbf{v}$ is artificially imposed for numerical stability of the explicit method [72], but is not needed in the quasi-static method. In three dimensions, this term induces a restriction on the timestep $\Delta t \leq \frac{h^2}{6\kappa}$. Hence, if κ is viewed as a physical constant, this condition is more restrictive than the CFL condition. However, for stability, it is sufficient to choose κ as scaling linearly with the grid spacing, in which case the timestep restriction scales in the same way as the CFL condition.

An explicit forward Euler discretization of Eq. 1 reads

$$\frac{\boldsymbol{\sigma}^{n+1} - \boldsymbol{\sigma}^n}{\Delta t} = -\left(\mathbf{v}^n \cdot \nabla\right) \boldsymbol{\sigma}^n + \left(\mathbf{L}^{\mathsf{T}}\right)^n \boldsymbol{\sigma}^n + \boldsymbol{\sigma}^n \mathbf{L}^n + \mathrm{Tr}(\mathbf{L}^n) \boldsymbol{\sigma}^n + \mathbf{C} : \left(\mathbf{D}^n - \frac{D^{\mathrm{pl}}}{\bar{s}^n} \boldsymbol{\sigma}_0^n\right). \tag{24}$$

3.3. Quasi-static method

We now formulate a specific three-dimensional projection method for solving Eq. 1 subject to the quasi-static constraint Eq. 3. We first neglect the $\mathbf{C} : \mathbf{D}$ term in Eq. 1 and compute an intermediate stress $\boldsymbol{\sigma}^*$,

$$\boldsymbol{\sigma}^* = \boldsymbol{\sigma}^n + \Delta t \left(\left(\mathbf{L}^{\mathsf{T}}\right)^n \boldsymbol{\sigma}^n + \boldsymbol{\sigma}^n \mathbf{L}^n - \mathrm{Tr}(\mathbf{L}^n) \boldsymbol{\sigma}^n - \mathbf{C} : \left(\frac{D^{\mathrm{pl}}}{\bar{s}^n} \boldsymbol{\sigma}_0^n\right)\right). \tag{25}$$

If the velocity at the next timestep $\mathbf{v}^{n+1}$ were known, we could compute

$$\mathbf{D}^{n+1} = \frac{1}{2}\left(\left(\nabla \mathbf{v}^{n+1}\right) + \left(\nabla \mathbf{v}^{n+1}\right)^{\mathsf{T}}\right) \tag{26}$$

and complete the forward Euler step in Eq. 25 as

$$\boldsymbol{\sigma}^{n+1} = \boldsymbol{\sigma}^{*} + \Delta t \left(\mathbf{C} : \mathbf{D}^{n+1}\right). \tag{27}$$

Taking the divergence of Eq. 27 and rearranging terms leads to the equation

$$\Delta t \nabla \cdot \left(\mathbf{C} : \mathbf{D}^{n+1}\right) = -\nabla \cdot \boldsymbol{\sigma}^{*}. \tag{28}$$

Equation 28 is a linear system for the velocity $\mathbf{v}^{n+1}$ involving mixed spatial derivatives. The source term is given by $-\nabla \cdot \boldsymbol{\sigma}^{*}$. After solving for $\mathbf{v}^{n+1}$, it can be used to compute $\boldsymbol{\sigma}^{n+1}$ via Eq. 27. Through this process, $\boldsymbol{\sigma}^{*}$ is projected back to be divergence-free, arriving at $\boldsymbol{\sigma}^{n+1}$.

The mixed derivatives in Eq. 28 increase the complexity of the projection for hypo-elastoplasticity when compared to the Poisson problem in fluid dynamics, but Eq. 28 can nevertheless be solved rapidly via standard techniques of numerical linear algebra such as the multigrid method. The multigrid method relies on the Gauss–Seidel method for iterative smoothing of the solution, and Gauss–Seidel smoothing is guaranteed to converge if either the linear system is (A) weakly diagonally dominant, or (B) symmetric positive definite. In general the linear system in Eq. 28 will not satisfy condition A, but will satisfy condition B. Hence Gauss–Seidel smoothing is guaranteed to converge, which we use as a component in a multigrid method—details of this multigrid solver are presented later. A connection to the general continuous-time framework presented in Sec. 2.4 is provided in Appendix A.

3.4. Discretization and finite difference stencils

The evolution equation for the stress, Eq. 1, depends on spatial derivatives of the velocity, while the equation satisfied by the velocity, Eq. 2, depends on spatial derivatives of the stress. We exploit this structure through a staggered grid with uniform spacing $\Delta x = \Delta y = \Delta z = h$. The stress tensor $\boldsymbol{\sigma}$ and effective temperature χ are stored at cell centers and indexed by half-integers, while the velocity $\mathbf{v}$ is stored at cell corners and indexed by integers, as shown in Fig. 2(b).

Let $(\partial f/\partial x)_{i,j,k}$ denote the partial derivative of a field f with respect to x evaluated at grid point (i, j, k). The staggered centered difference is

$$\begin{aligned}\left(\frac{\partial f}{\partial x}\right)_{i+\frac{1}{2},j+\frac{1}{2},k+\frac{1}{2}} = \frac{1}{4h}\Big(&f_{i+1,j,k} - f_{i,j,k} + f_{i+1,j+1,k} - f_{i,j+1,k} \\ &+ f_{i+1,j,k+1} - f_{i,j,k+1} + f_{i+1,j+1,k+1} - f_{i,j+1,k+1}\Big).\end{aligned} \tag{29}$$

Equation 29 averages four edge-centered centered differences surrounding the cell center and has a discretization error of size $\mathcal{O}(h^2)$. The derivative at a cell corner is obtained by

the replacement $(i,j,k) \to (i-\frac{1}{2}, j-\frac{1}{2}, k-\frac{1}{2})$. The diffusive term appearing in the velocity update in Eq. 23 is computed via the standard center-difference formula,

$$\left(\frac{\partial^2 f}{\partial x^2}\right)_{i,j,k} = \frac{f_{i+1,j,k} - 2f_{i,j,k} + f_{i-1,j,k}}{h^2}. \tag{30}$$

The advective derivatives in Eqs. 23 & 24 must be upwinded for stability; we use the second-order essentially non-oscillatory (ENO) scheme [73]. With $[f_{xx}]_{i,j,k}$ denoting the second derivative with respect to x of the field f at grid point (i,j,k) computed using Eq. 30, the ENO derivative is defined in the x direction as

$$\left(\frac{\partial f}{\partial x}\right)_{i,j,k} = \frac{1}{2h}\begin{cases} -f_{i+2,j,k} + 4f_{i+1,j,k} - 3f_{i,j,k} & \text{if } u_{i,j,k} < 0 \text{ and } \left|[f_{xx}]_{i,j,k}\right| > \left|[f_{xx}]_{i+1,j,k}\right|, \\ 3f_{i,j,k} - 4f_{i-1,j,k} + f_{i-2,j,k} & \text{if } u_{i,j,k} > 0 \text{ and } \left|[f_{xx}]_{i,j,k}\right| > \left|[f_{xx}]_{i-1,j,k}\right|, \\ f_{i+1,j,k} - f_{i-1,j,k} & \text{otherwise.} \end{cases} \tag{31}$$

Equation 31 uses the curvature of f to switch between an upwinded three-point derivative and a centered difference. Versions of Eqs. 29, 30, & 31 in the y and z coordinates are obtained analogously.

To solve Eq. 28 via numerical linear algebra, the spatial derivatives must first be discretized using finite differences. In addition to the finite differences discussed above, Eq. 28 also contains mixed partial derivatives. The xy-derivative is computed numerically as

$$\left(\frac{\partial^2 f}{\partial x \partial y}\right)_{i,j,k} = \frac{f_{i+1,j+1,k} - f_{i+1,j-1,k} - f_{i-1,j+1,k} + f_{i-1,j-1,k}}{4h^2}, \tag{32}$$

with analogous expressions for other mixed partials.

3.5. Parallelization via MPI and domain decomposition

We solve Eqs. 23 & 24 in parallel using a custom implementation written in C++ and using the MPI library for parallelization [74]. The global grid is split into smaller subgrids, each of which is assigned to an individual processor (Fig. 2(a)). The finite difference stencils in Eqs. 29 & 30 require data from adjacent gridpoints, and the ENO derivative in Eq. 31 requires data from at most two grid points away. On grid points within two points of a subdomain boundary, the derivative calculation can therefore require inaccessible data in a distributed memory setting.

To handle this, we pad each processor subdomain with "ghost regions" of width two. A ghost region is a cubical shell of non-physical grid points whose field values are filled with data from adjacent processors, so that each subdomain can freely and locally access information computed and stored in adjacent subdomains (Fig. 3). At the simulation boundaries, ghost regions are used to enforce boundary conditions. For periodic boundary conditions, the ghost regions wrap around to processor subdomains on the other side of the simulation. For non-periodic conditions, the ghost grid points store whatever values enforce the desired boundary conditions.

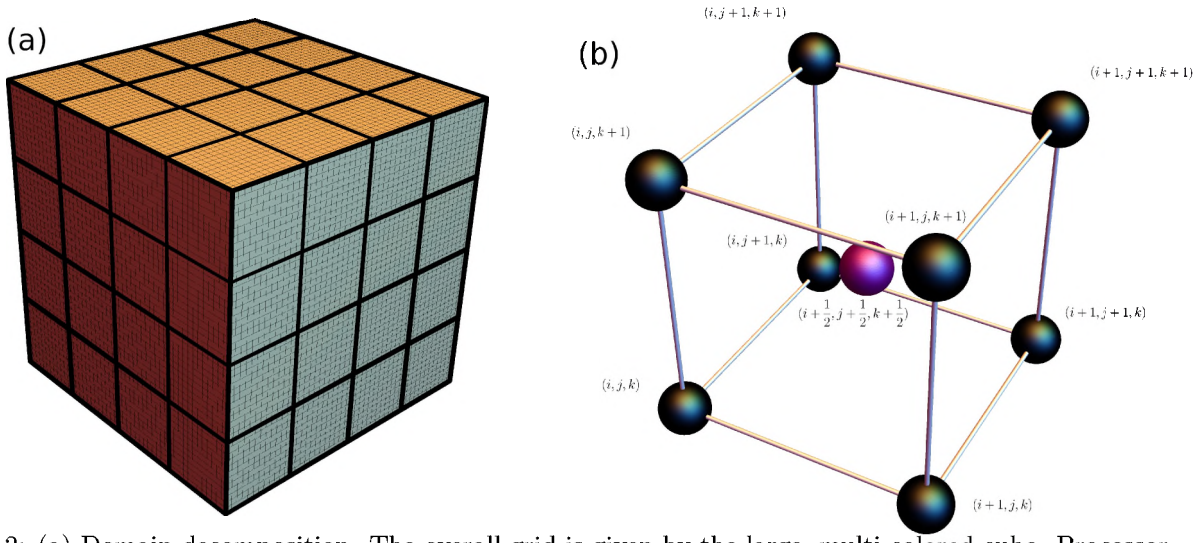

Figure 2: (a) Domain decomposition. The overall grid is given by the large, multi-colored cube. Processor subdomains are delimited by the thick black markings separating the global grid into a $4 \times 4 \times 4$ grid of smaller cubes. The fine black lines denote individual grid cells, which are further amplified in the depiction of the staggered grid to the right. (b) The staggered arrangement of fields on the grid. The cube here corresponds to to a single grid cell of side length h. Velocities $\mathbf{v}$ are stored at cell corners denoted by black spheres. Stresses $\boldsymbol{\sigma}$ and effective temperatures χ are stored at cell centers indicated by the purple sphere. First-order velocity derivatives are required to update the stress; by averaging the four available centered differences surrounding the center of the cell, we obtain a second-order staggered stencil. The same arrangement arises for computing stress derivatives at the cell corners in the velocity update.

At the start of each timestep, each processor communicates with 26 nearby processors via non-blocking communication, sharing six faces, twelve edges, and eight corner regions. Each processor sends data to nearby processors, receives the data it requires from the same nearby processors, and loads that data into its ghost regions. The total cost of parallel communication scales with the surface area of a processor subdomain. To reduce the overhead, we compute a decomposition into rectangular regions that minimizes the surface area.

3.6. Performing the projection step

We solve Eq. 28 for the velocity using a custom parallel implementation of the geometric multigrid method, a multi-resolution linear system solver that is particularly suited to elliptic problems that take place on a physical grid [75]. Let G_0 be the original grid, and let $\mathbf{A}_0\mathbf{x}_0 = \mathbf{b}_0$ be the linear system to solve on this grid. In the multigrid method, a hierarchy of progressively coarser grids $G_1, G_2, \ldots, G_g$ is introduced. In our implementation, if G_k has resolution $Q_k \times M_k \times N_k$, then G_{k+1} has resolution $\lceil Q_k/2 \rceil, \lceil M_k/2 \rceil, \lceil N_k/2 \rceil$. Interpolation operators $\mathbf{T}_k : G_k \to G_{k-1}$ are introduced based on linear interpolation, and restriction operators $\mathbf{R}_k : G_k \to G_{k+1}$ are introduced based on local averaging. Both $\mathbf{T}_k$ and $\mathbf{R}_k$ can be represented as rectangular matrices, and in our implementation $\mathbf{R}_{k-1} = \mathbf{T}_k^{\mathsf{T}}$—this condition is not necessary for a practical implementation, but is useful in some convergence proofs [21].

Our multigrid implementation uses the standard V-cycle [20, 21] with two pre-smoothing steps and two post-smoothing steps. On G_0 the grid is decomposed among the processors in

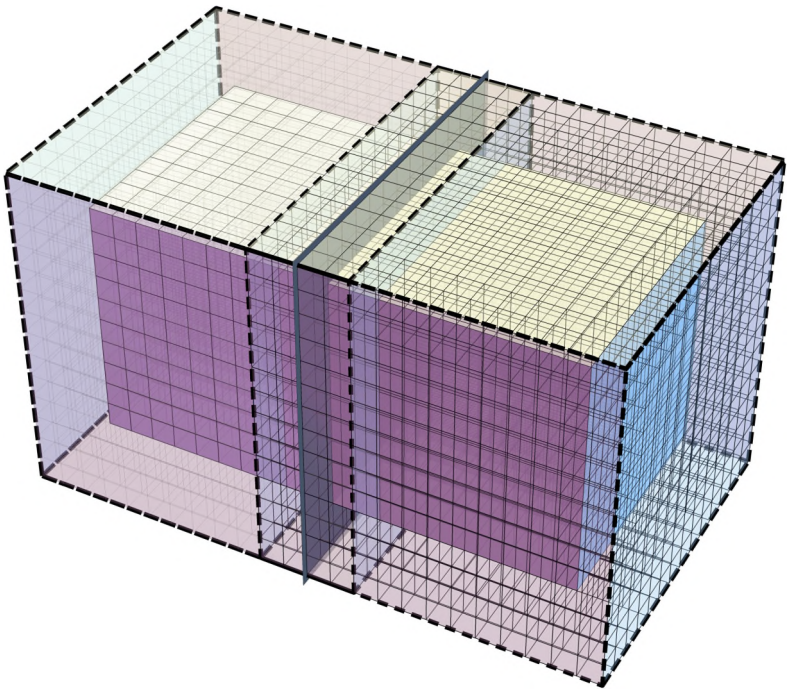

Figure 3: Processor ghost regions. The two solid cubes represent two adjacent processor subdomains; the boundary between them is indicated by a gray plane in the center of the figure. Surrounding each processor subdomain is a transparent two-grid-point ghost region bounded by black dashed lines. For clarity, the ghost region grid in the left processor subdomain has been drawn in a thin gray, while the ghost region grid in the right processor subdomain has been drawn in black. These two processors communicate the overlapping rectangular strip surrounding the separating plane in the center of the figure.

the same way as the simulation fields (Fig. 2(b)). The smoothing steps are performed using the Gauss–Seidel method on each processor, with the ghost regions being synchronized after each step. This requires building a representation of the linear system on each grid, which we do via recursive matrix multiplication [76, 77],

$$\mathbf{A}_k = \mathbf{R}_{k-1}\mathbf{A}_{k-1}\mathbf{T}_k. \tag{33}$$

The implementation works with periodic and non-periodic boundary conditions, and arbitrary grid dimensions. As the grids are coarsened, the amount of work on each grid is rapidly reduced, to the point where it is no longer effective for all processors to share the work. The implementation therefore has the ability to amalgamate the coarser problem onto a smaller set of processors, with the rest remaining idle.

The multigrid implementation uses C++ templates, so that the linear system can be compiled to work with an arbitrary data type. For the current problem, $\mathbf{b}_0$ is given by the source term $-\Delta t \nabla \cdot \boldsymbol{\sigma}$ and $\mathbf{x}_0$ contains values of $\mathbf{v}^{n+1}$ across the entire grid. Hence, we compile the multigrid library where the elements of $\mathbf{b}_0$ and $\mathbf{x}_0$ are 3-vectors, and the elements of $\mathbf{A}_0$ are 3×3 symmetric matrices. The matrix $\mathbf{A}_0$ is sparse, and a grid point (i, j, k) is only coupled to the 27 grid points in the $3 \times 3 \times 3$ surrounding cube of grid points given by coordinates $(i + \{-1, 0, 1\}, j + \{-1, 0, 1\}, k + \{-1, 0, 1\})$ in our discretization scheme.

4. Shearing between two parallel plates

In the following sections, we consider several material samples being sheared between two parallel plates. This example is experimentally relevant, has simple boundary conditions, demonstrates complex shear banding dynamics [43, 42, 44, 45, 47, 35, 34, 46], and has been studied previously in two dimensions [23]. It represents a natural physical scenario to compare three dimensional results to two dimensional results, compare simulation data to experiments, and to quantitatively compare the explicit and quasi-static methods.

The domain occupies $-L \leq x < L, -L \leq y < L$, and $-\gamma L \leq z \leq \gamma L$ with $\gamma = \frac{1}{2}$ and $L = 1$ cm. A natural unit of time is given as $t_s = L/c_s$ where $c_s = \sqrt{\mu/\rho}$ is the material shear wave speed, and we measure time in this scale. In all simulations, we consider a domain periodic in the x and y directions with shear velocity applied on the top and bottom boundaries in z. The boundary conditions are given by

$$\mathbf{v}(x, y, \pm\gamma L, t) = (\pm U(t), 0, 0), \tag{34}$$

where the function $U(t)$ is given by

$$U(t) = \begin{cases} \frac{U_B t}{t_s} & \text{if } t < t_s, \\ U_B & \text{otherwise.} \end{cases} \tag{35}$$

The ramp-up in the function $U(t)$ prevents a large deformation rate near the boundary that would be present with $U(t) = U_B$ immediately at $t = 0$. The elasticity and plasticity parameters are defined in Table 1. From these values, the natural timescale is $t_s = 4.05$ µs.

A diagram of the global three-dimensional grid and the ghost regions at simulation boundaries used for implementing the boundary conditions is shown in Fig. 4. The cell-cornered grid points run according to $i \in \{0, \dots, Q-1\}$, $j \in \{0, \dots, M-1\}$, and $k \in \{0, \dots, N\}$; because the grid is non-periodic in z there is an extra grid point in this direction. The velocities at grid points with $k = 0$ and $k = N$ are fixed according to the boundary velocity in Eq. 34. The cell-centered grid points run according to $i \in \{\frac{1}{2}, \frac{3}{2}, \dots Q - \frac{1}{2}\}$, $j \in \{\frac{1}{2}, \frac{3}{2}, \dots M - \frac{1}{2}\}$, and $k \in \{\frac{1}{2}, \frac{3}{2}, \dots N - \frac{1}{2}\}$. Ghost layers of cell-centered grid points are at $(i, j, -\frac{1}{2})$, $(i, j, -\frac{3}{2})$, $(i, j, N + \frac{1}{2})$, and $(i, j, N + \frac{3}{2})$. The values of $\boldsymbol{\sigma}$ and χ in the ghost layers are linearly interpolated from the two most adjacent layers, to ensure that these fields remain free on the boundary. At the simulation boundaries in the x and y directions, ghost points outside the simulation domain are filled with values that wrap around.

In each case considered in the following sections, the physics of the material sample is encoded in the initial effective temperature distribution $\chi(\mathbf{x}, t = 0)$. Following the introduction in Sec. 3.1, χ is a continuum-scale variable that encodes the density of STZs, and hence its initial condition affects the future evolution of plastic deformation within the material.

4.1. Qualitative comparison between explicit and quasi-static methods

We now demonstrate the qualitative equivalence between results computed with the explicit and quasi-static methods. We consider an initial condition corresponding to a finite cylindrical inclusion

$$\chi(\mathbf{x}, t = 0) = 600 \text{ K} + (200 \text{ K}) e^{-500(z^2+y^2)/L^2}, \tag{36}$$

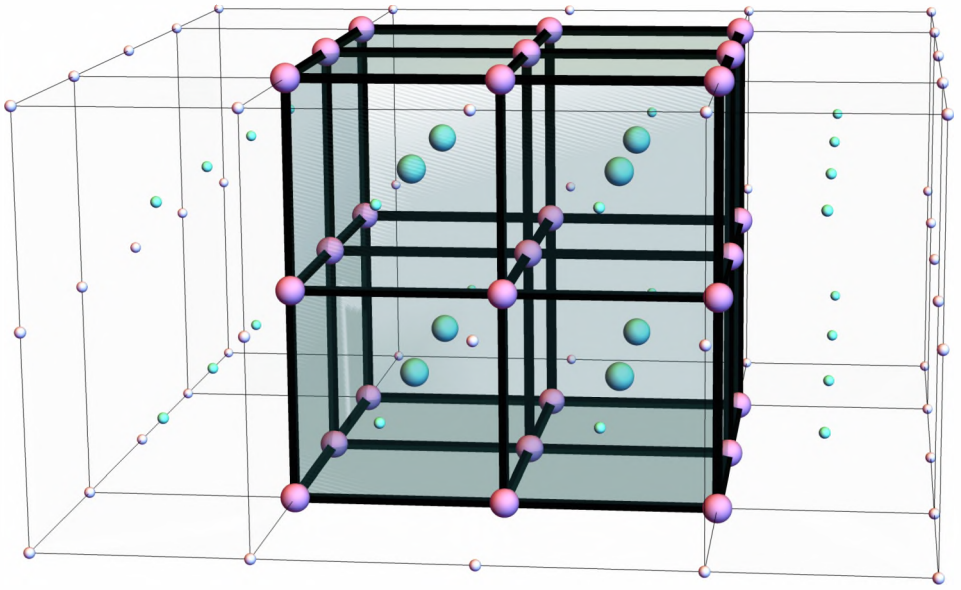

Figure 4: A diagram of the simulation grid layout for the simplified case of $(Q, M, N) = (2, 2, 2)$. Corner-centered grid points are shown in pink and cell-centered grid points are shown in green. Ghost grid points used for enforcing boundary conditions are shown adjacent to the $\pm x$ faces and are surrounded by see-through rectangular prisms. For clarity, these are omitted from the $\pm z$ faces. Corner-centered ghost points and cell-centered ghost points are smaller and are shown in lighter pink and green than their physical counterparts. The ghost points adjacent to the $\pm x$ and $\pm y$ faces wrap around, and are used to enforce periodic boundary conditions. In the z direction, the ghost grid points are used to linearly interpolate the $\boldsymbol{\sigma}$ and χ values, leaving them effectively free. In the z direction, there is one extra corner-centered grid point, giving the appearance of a grid of size $2 \times 2 \times 3$. This grid point is used to enforce shear boundary conditions on the velocity field, but the equivalent cell-centered grid points are used to store ghost $\boldsymbol{\sigma}$ and χ values.

for $x > -L/2$ and $x < L/2$, and 600 K otherwise. Initially the cylindrical inclusion is slightly more amenable to plastic deformation, and hence we expect to see a shear band nucleate from it. To visualize the effective temperature field in three dimensions, we use a custom opacity function defined as

$$O(\mathbf{x}) = \begin{cases} \left(\frac{\chi(\mathbf{x})-\chi_{bg}}{\chi_\infty-\chi_{bg}}\right) & \text{if } \frac{\chi(\mathbf{x})-\chi_{bg}}{\chi_\infty-\chi_{bg}} > \frac{1}{2}, \\ \exp\left(-a\left(\frac{\chi_\infty-\chi_{bg}}{\chi(\mathbf{x})-\chi_{bg}}\right)^\eta\right) & \text{otherwise.} \end{cases} \tag{37}$$

Equation 37 sets the opacity of a grid point based on the value of $\chi(\mathbf{x})$. The parameters a and η are chosen on a case-by-case basis to reveal the most interesting features[2]. The initial condition is depicted in Fig. 5. The grid is of size $64 \times 64 \times 32$ to accommodate the limitations of the explicit simulation method, corresponding to a grid spacing $h = \frac{L}{32}$.

[2]Ideally, we would like to use the same opacity parameters for all plots. However, due to significant variations in the ranges of the χ fields and their spatial structures, we found it was necessary to set the parameters on an individual basis. We note, however, that the color scale is absolute across all simulations.

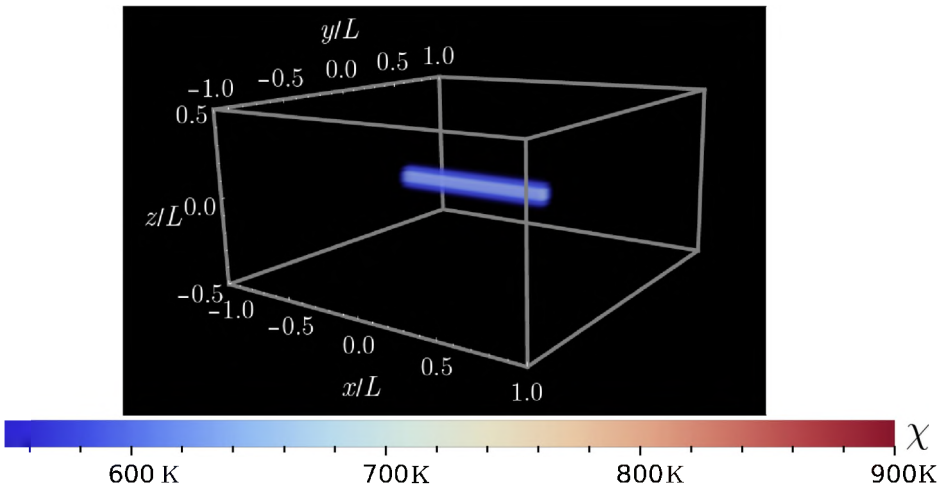

Figure 5: The effective temperature field χ in the initial configuration for the quasi-static to explicit method quantitative comparison. Here, $a = 0.25$ and $\eta = 0.5$ in the opacity function.

A viscous stress constant of $\kappa = 0.15\frac{L^2}{t_s}$ was used in Eq. 23. The timestep for the explicit method is $\Delta t_{\mathrm{e}} = \frac{h^2 t_s}{20L^2}$.

A typical applied shear velocity that is comparable to a realistic loading rate in a laboratory experiment is $U_b = 10^{-7}L/t_s$ [43]. With this velocity, running an explicit simulation is prohibitively expensive due to the CFL condition. To ensure that significant plastic deformation occurs on timescales reachable by the explicit method, a scaling parameter ζ is introduced. The molecular vibration timescale τ_0 is rescaled to $\tau_0\zeta^{-1}$ and the applied shear velocity is inversely rescaled to $U_B = 10^{-7}L/t_s\zeta$. The simulation is conducted until a final time of $t_f = 2 \times 10^6 t_s/\zeta$. As ζ approaches zero, the quasi-static limit of Eqs. 1 & 2 is formally approached. We therefore expect greater agreement for smaller values of ζ. Due to the appearance of $\frac{1}{\tau_0}$ in Eq. 19, the introduction of ζ has the effect of linearly scaling the magnitude of plastic deformation by a factor of ζ. A quasi-static timestep of $\Delta t_{\mathrm{qs}} = 200 t_s/\zeta$ is used.

In Fig. 6, we show three snapshots of the effective temperature field from each of the two simulation methods, at $t = 50t_s$, $t = 75t_s$, and $t = 100t_s$ respectively. The explicit simulation is shown on the left and the quasi-static simulation is shown on the right. The results are qualitatively similar in all three snapshots. At $t = 50t_s$, a shear band begins to emerge, nucleating outwards from the center of the simulation. A thin region of higher χ is visible in the center of the band. By $t = 75t_s$, the shear band has fully formed and spans the system. At $t = 100t_s$, the band grows stronger and χ continues to increase.

Figure 7 shows cross-sections in z for fixed $x = 0$ and $y = 0$ of $\|\boldsymbol{\sigma}_0\|_{\mathrm{qs}} - \|\boldsymbol{\sigma}_0\|_{\mathrm{e}}$ for several time points before the onset of plastic deformation, highlighting some differences between the two methods. The explicit simulation exhibits oscillations due to elastic waves propagating through the medium. Because the quasi-static method does not resolve these elastic waves, the oscillations are apparent in the deviatoric stress differences. When plastic deformation

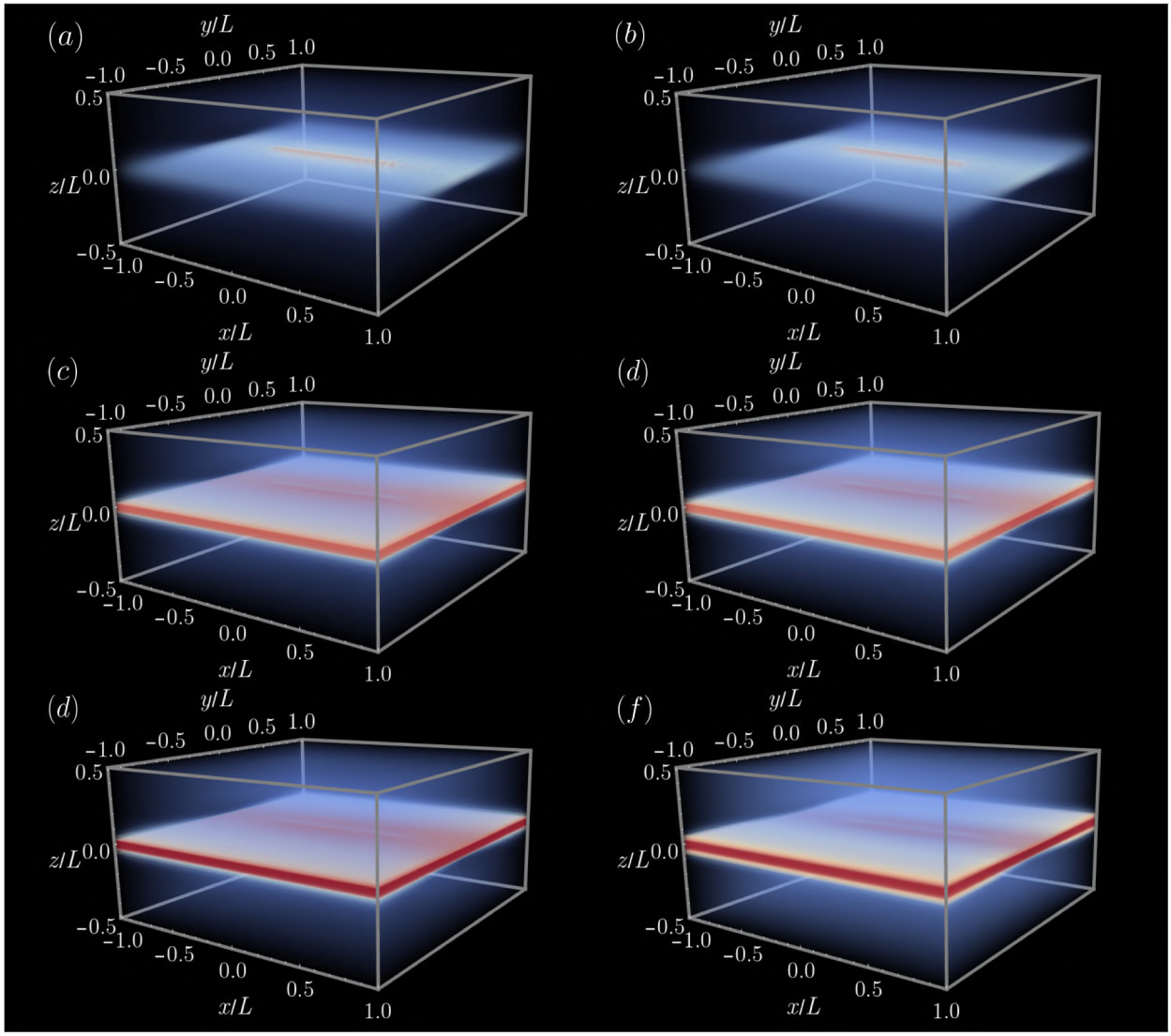

Figure 6: Snapshots of the effective temperature distribution $\chi(\mathbf{x}, t)$ for the explicit simulation (left) and quasi-static simulation (right) for $\zeta = 10^4$. The simulation fields are qualitatively similar. In all plots, $a = 0.4$ and $\eta = 1.4$ in the opacity function. (a,b) $t = 50t_s$. (c,d) $t = 75t_s$. (e,f) $t = 100t_s$. The colorbar is the same as in Fig. 5.

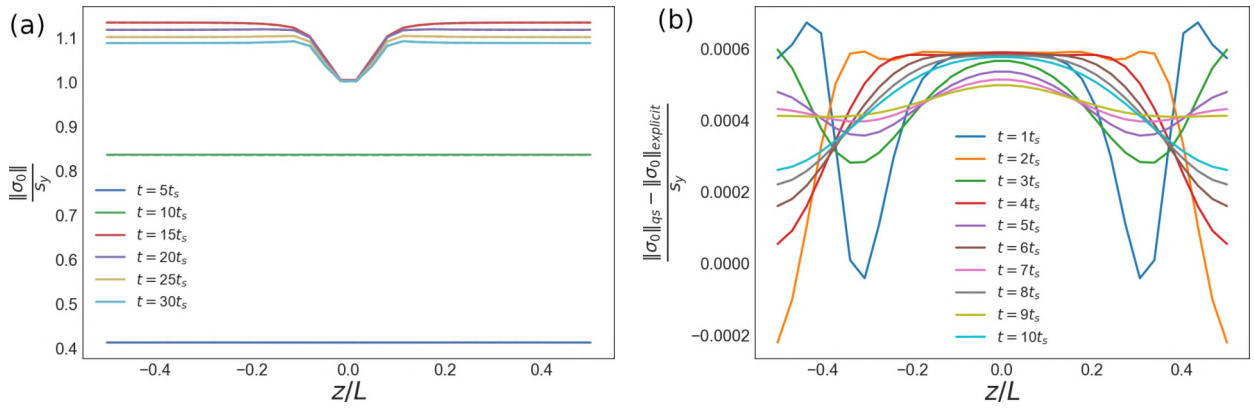

Figure 7: (a) The magnitude of the deviatoric stress tensor $\|\boldsymbol{\sigma}_0\|$ for the explicit and quasi-static simulation methods along a cross section in z for $x = 0$ and $y = 0$ fixed. Results for the explicit and quasi-static simulation methods are shown in dashed and solid lines respectively. Oscillations at $t = 5t_s$ and $t = 10t_s$ are due to elastic waves propagating through the medium in the explicit simulation, but are difficult to see by eye at this scale, see (b). As plasticity kicks in past $t = 15t_s$, these waves damp out. (b) The difference in the magnitude of the deviatoric stress tensor $\|\boldsymbol{\sigma}_0\|$ for the explicit and quasi-static simulation methods, along a cross section in z for $x = 0$ and $y = 0$ fixed. The oscillations are due to elastic waves propagating through the medium in the explicit simulation.

sets in, plasticity-induced damping removes the elastic waves and the agreement improves.

4.2. Quantitative comparison between explicit and quasi-static methods

Having demonstrated the qualitative agreement between the two simulation methodologies for $\zeta = 10^4$ in the previous section, we now examine convergence as ζ is decreased. The same simulation geometry, boundary conditions, and initial conditions in the effective temperature field are used here as in the previous section. To quantitatively compute the agreement between the explicit and quasi-static methods, we define a norm on simulation fields $\mathbf{f}$,

$$\|\mathbf{f}\|(t) = \sqrt{\frac{1}{8\gamma L^3}\int_{-\gamma L}^{\gamma L}\int_{-L}^{L}\int_{-L}^{L}|\mathbf{f}(\mathbf{x},t)|^2\,dx\,dy\,dz}. \tag{38}$$

The integral in Eq. 38 runs over the entire simulation domain and is computed numerically via the trapezoid rule. The appearance of $|\cdot|$ in Eq. 38 is taken to be the Euclidean norm for vectors, absolute value for scalars, and the Frobenius norm for matrices.

Explicit and quasi-static simulations were carried out for values of $\zeta = 10^4, 5\times10^3, 2.5\times10^3$ and 1.25×10^3. Equation 38 was evaluated for $\chi_{\text{qs}} - \chi_{\text{e}}$, $\boldsymbol{\sigma}_{\text{qs}} - \boldsymbol{\sigma}_{\text{e}}$, and $\mathbf{v}_{\text{qs}} - \mathbf{v}_{\text{e}}$ at intervals of $0.02t_s$. The norm in χ is measured in terms of χ_∞, the norm in $\boldsymbol{\sigma}$ is measured in terms of s_Y, and the norm in $\mathbf{v}$ is measured in terms of U_B to ensure all values are of order unity. The explicit timestep was $\Delta t_{\text{e}} = \frac{t_s h^2}{20L^2}$ and the quasi-static timestep was $\Delta t_{\text{qs}} = \frac{100t_s}{\zeta}$ for each simulation.

Plots of all three norm values are shown as a function of time in Fig. 8(a) for the value of $\zeta = 1.25\times10^3$. Oscillations due to elastic waves are visible in all simulation fields until

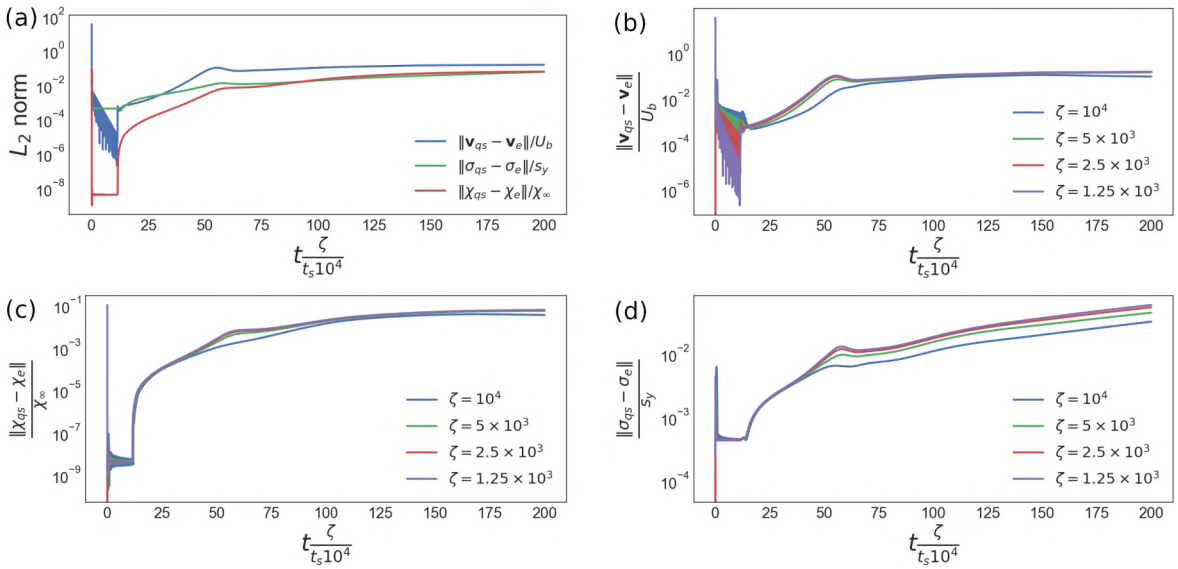

Figure 8: L_2 norm of the χ, $\mathbf{v}$, and $\boldsymbol{\sigma}$ simulation field differences between the explicit and quasi-static method computed using Eq. 38 and normalizing by the respective characteristic variables as defined in the text, for different values of ζ. (a) A comparison of the four different field norms, for the values of $\zeta = 10^4$. The remaining three panels show the differences in (b) velocity, (c) effective temperature, and (d) stress, respectively, for a range of values of ζ.

around $t \approx 12t_s$ when the yield stress is reached. After the onset of plastic deformation, the norm in effective temperature increases steadily, most rapidly during the period of shear band nucleation from $t \approx 12t_s$ to $t \approx 25t_s$. The disagreements in $\boldsymbol{\sigma}$ and $\mathbf{v}$ decrease during the elastic region, and steadily increase after plastic deformation begins.

Figures 8(b), 8(c), and 8(d) show the quantitative comparisons as a function of time for values of $\zeta = 10^4, 5 \times 10^3, 2.5 \times 10^3$, and 1.25×10^3 for $\mathbf{v}$, χ, and $\boldsymbol{\sigma}$ respectively. In all plots, better agreement with smaller ζ is observed during the elastic regime and during the onset of plasticity while $t \leq 12t_s$. After shear band nucleation from $12t_s \leq t \leq 25t_s$, all values of ζ have roughly equal error magnitudes, with slightly greater agreement for higher values of ζ. This is consistent with previous comparisons in two dimensions, where the dominant factor governing the disagreement between the two simulation methods was shown to be due to differences in the discretization rather than the value of ζ itself [23].

A method to reduce the differences in discretization is to increase the background χ field. With higher values of background χ, finer-scale features in the shear banding dynamics are less prominent. This ensures that differences in the spatial discretization will be minimized. There is also less rapid development of the shear band, and thus the difference in timestep between the two methods will be less significant. Snapshots of the effective temperature field are shown in Fig. 9 at $t = 10^6 t_s$ for background χ field of $\chi_{\text{bg}} = 600$ K, 650 K, 700 K. Figure 10 confirms that the differences between the two types of simulation decreases as χ_{bg} increases.

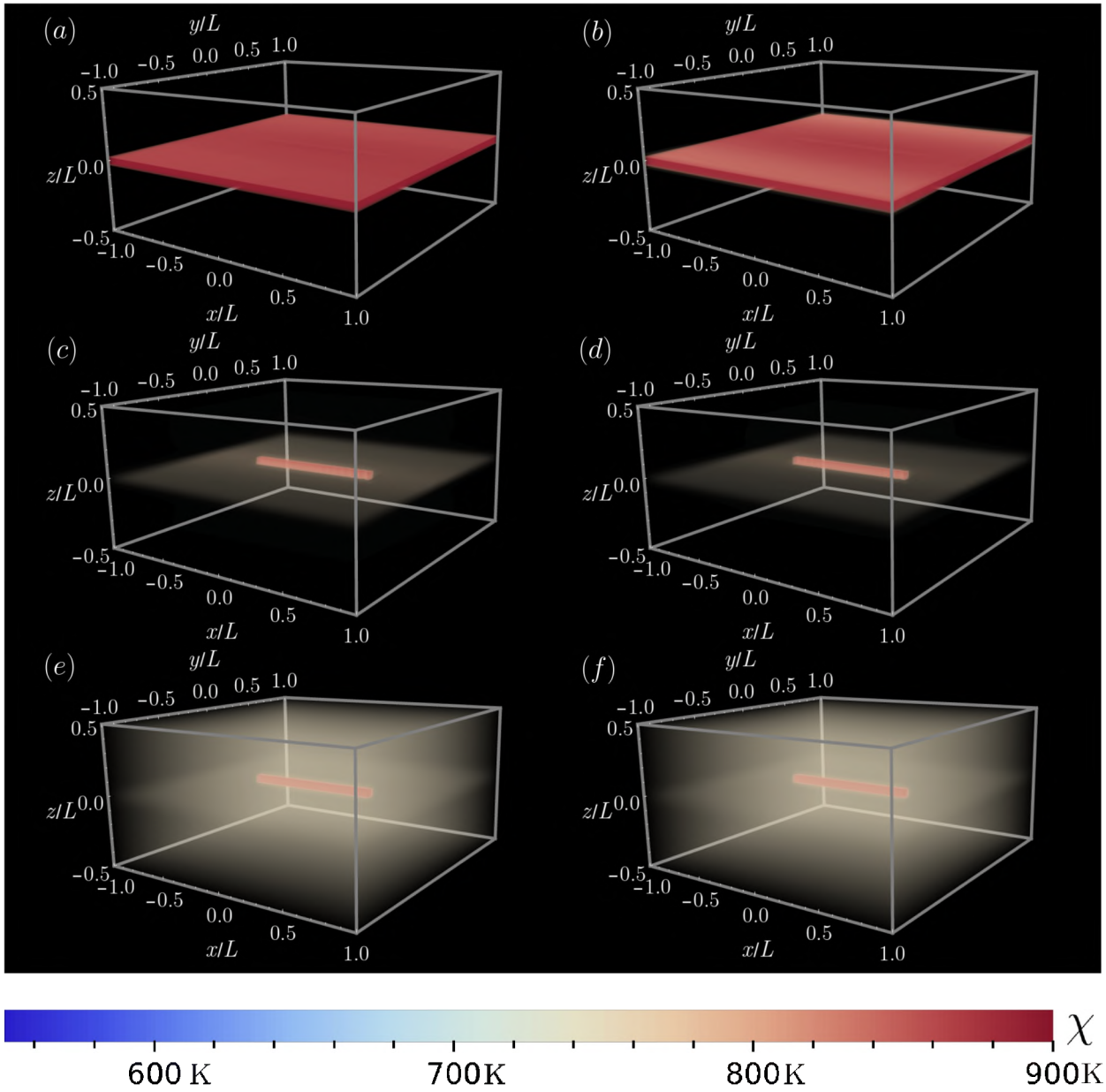

Figure 9: Qualitative demonstration of the effect of increasing the background χ field with χ_{bg} set to (a/b) 600 K (c/d) 650 K and (e/f) 700 K. All snapshots are displayed at $t = 10^6 t_s$ for a value of $\zeta = 10^4$, with fixed values of $a = 0.75$ and $\eta = 3$ in the opacity function. Simulation results are shown for the explicit method on the left and the quasi-static method on the right. For lower χ_{bg}, the shear band is more prominent, develops more rapidly, and has more fine-scale features, ensuring that the differences in spatial and temporal discretizations become more pronounced.

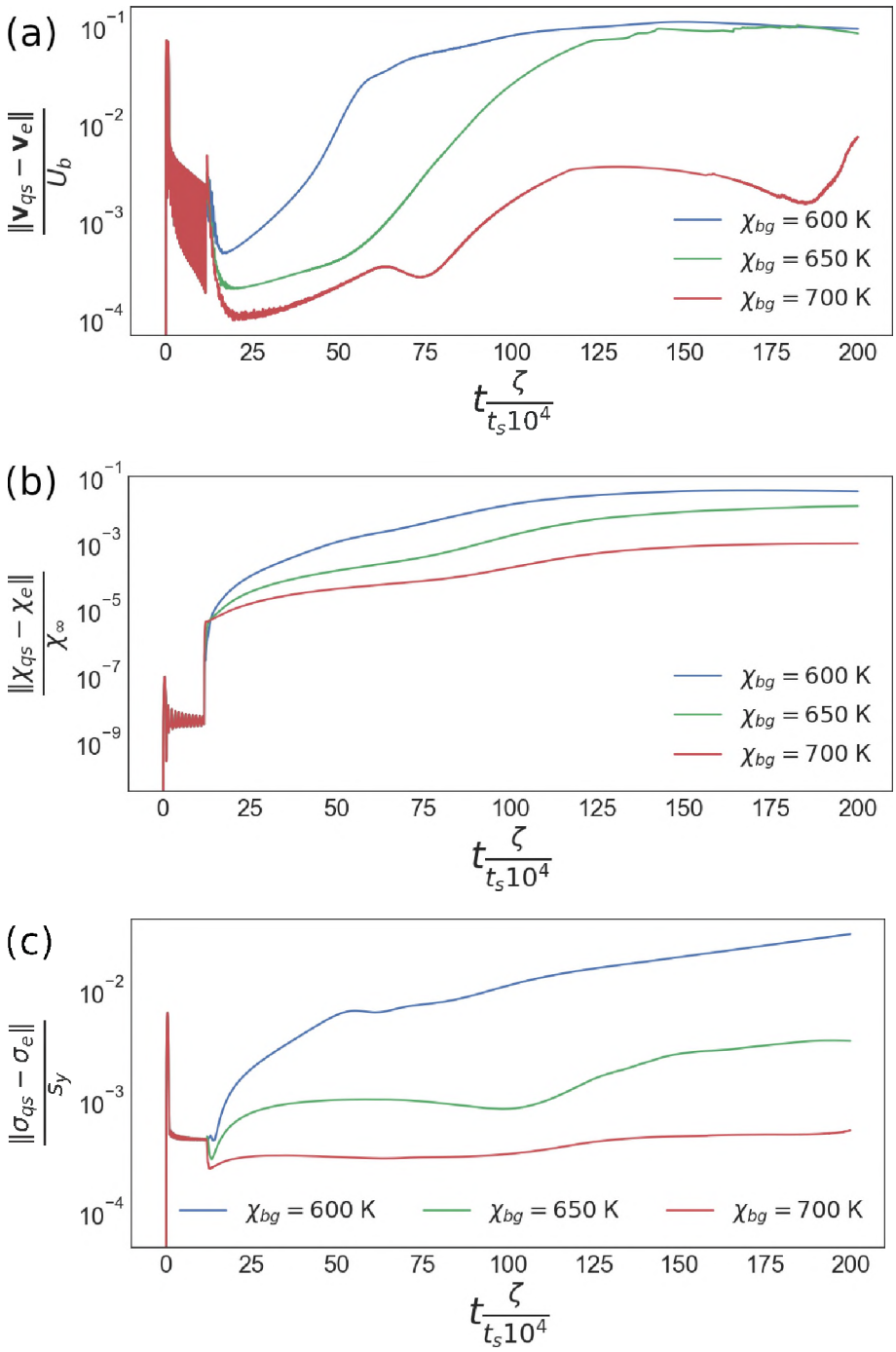

Figure 10: Normalized L_2 difference in (a) $\mathbf{v}$ (b) χ and (c) $\boldsymbol{\sigma}$ between the explicit and quasi-static methods for various choices of background χ field. Agreement improves as χ_{bg} increases due to a reduction in fine-scale features that differ between the two methods due to differences in the discretization.

4.3. Gaussian Defects

We now turn to simulating realistic physical timescales with the quasi-static method, where the scaling parameter is $\zeta = 1$. We first consider the nucleation of shear bands from localized imperfections of higher χ. Physically, this describes defects within the material structure which may be particularly susceptible to plastic deformation [78]. To begin, we consider a single defect, corresponding to an initial χ field of the form

$$\chi(\mathbf{x}, t = 0) = 550 \text{ K} + (170 \text{ K}) \exp\left(-200 \frac{\|\mathbf{x}\|^2}{L^2}\right). \tag{39}$$

The simulation was performed on a grid of size $256 \times 256 \times 128$, corresponding to a grid spacing of $h = L/128$. The length scale l appearing in Eq. 22 was fixed at $3h$ and sets the width of the shear bands. The boundary velocity was set to a value of $U_B = 5 \times 10^{-7} L/t_s$, and the simulation was conducted to a final time of $t_f = 4 \times 10^5 t_s$, using a quasi-static timestep of $\Delta t = 200 t_s$. For three-dimensional visualization, we use the opacity function from Eq. 37.

Snapshots of the effective temperature field at various time points are shown in Fig. 11. The initial condition is shown in Fig. 11(a). At $t = 10^5 t_s$ in Fig. 11(b), the defect has started to expand. By $t = 2 \times 10^5 t_s$ in Fig. 11(c), a shear band begins to nucleate, indicated by a quadrupolar structure emanating from the defect. The background χ field also begins to increase, as demonstrated by the presence of the transparent light blue background. By $t = 2.5 \times 10^5 t_s$ in Fig. 11(d), a distinct system-spanning band has become clear with a propagating front visible near its center. The band displays no curvature in either of the x or y directions. By $t = 150 t_s$ in Fig. 11(e), a prominent band has formed, and there is no longer a visible propagating front. The band continues to grow stronger and thicker through $t = 175 t_s$ in Fig. 11(f) and $t = 200 t_s$ (not shown).

We now introduce a second defect to highlight some three-dimensional characteristics of shear banding. We expect that their relative size and location will determine the dynamics, with the possibility of forming a single shear band that connects the two defects. The initial effective temperature field is

$$\chi(\mathbf{x}, t) = 550 \text{ K} + (200 \text{ K}) \left(\exp\left(-200 \frac{\|(\mathbf{x} - \mathbf{X}_1)\|^2}{L^2}\right) + \exp\left(-250 \frac{\|(\mathbf{x} - \mathbf{X}_2)\|^2}{L^2}\right)\right). \tag{40}$$

Two cases of Eq. 40 are considered. First, $\mathbf{X}_1 = (-0.5, -0.5, 0.35)$, $\mathbf{X}_2 = (-0.5, 0.5, 0.25)$, corresponding to two defects symmetric about the $y = 0$ plane with the same x coordinate, a slight offset in z, and different sizes. The results for this case using the same simulation parameters as Fig. 11 are shown in Fig. 12. Second, we take $\mathbf{X}_1 = (-0.5, -0.5, 0.35), \mathbf{X}_2 = (0.5, -0.5, 0.25)$; this is the same as the previous case, but with the roles of x and y interchanged. The results for this case again with the same grid size, quasi-static timestep, and boundary velocity as for the single defect are shown in Fig. 13.

There is an interesting contrast between the time-sequences displayed in Figs. 12 and 13. The initial configurations are shown in Figs. 12(a) and 13(a). Much like in the single defect simulations, $t = 50 t_s$ in Figs. 12(b) and 13(b) displays expansion of the defects, and $t = 100 t_s$

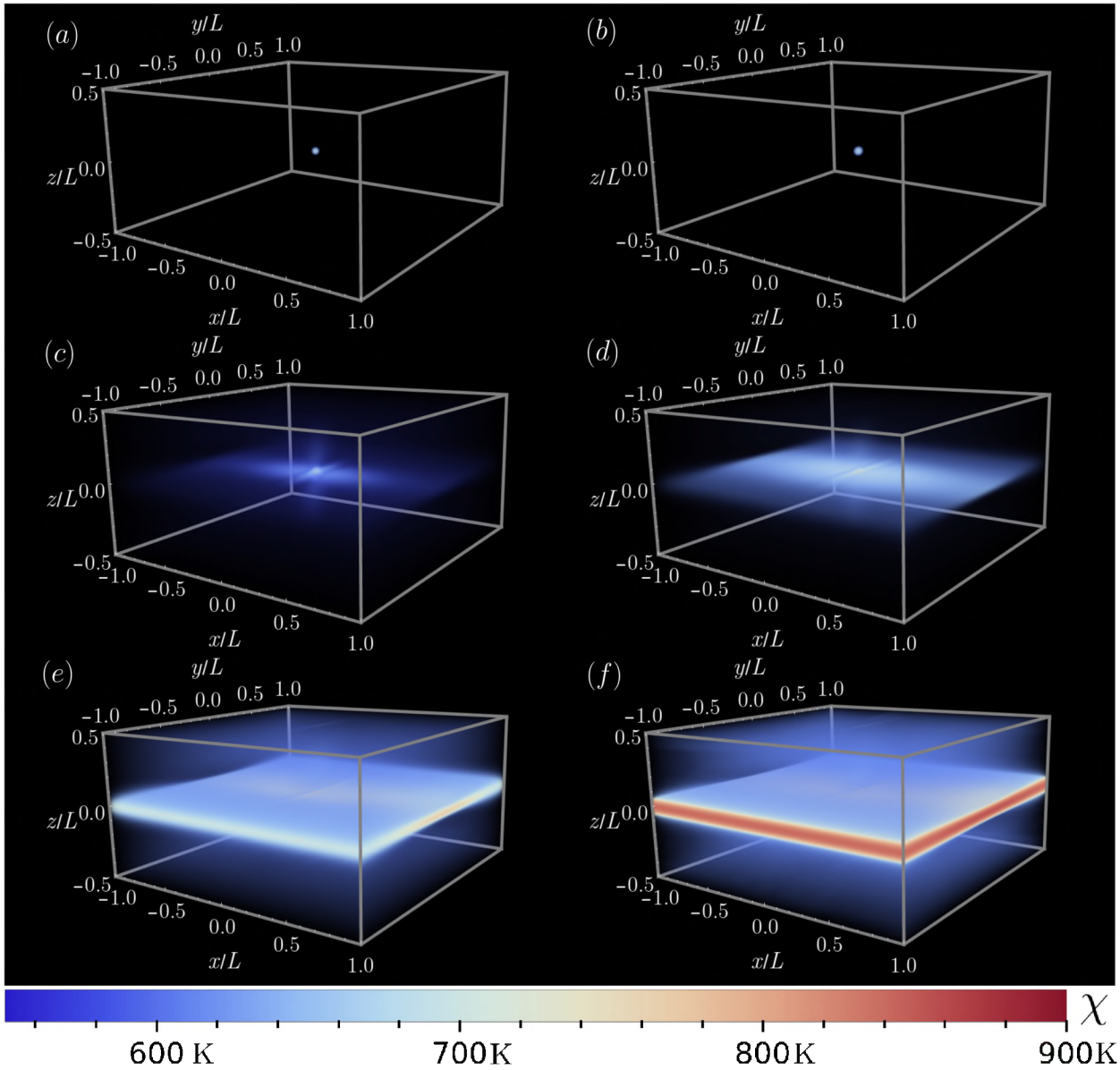

Figure 11: Snapshots of the effective temperature distribution $\chi(\mathbf{x}, t)$ for a quasi-static simulation with $\zeta = 1$. The initial condition is given in Eq. 39, corresponding to a small Gaussian defect at the center of the material. $a = 0.35$ and $\eta = 1.1$ for plots (a)–(c). $a = 0.4$ and $\eta = 1.4$ for plots (d)–(f). (a) $t = 0t_s$. (b) $t = 10^5 t_s$. (c) $t = 2 \times 10^5 t_s$. (d) $t = 2.5 \times 10^5 t_s$. (e) $t = 3 \times 10^5 t_s$. (f) $t = 4 \times 10^5 t_s$.

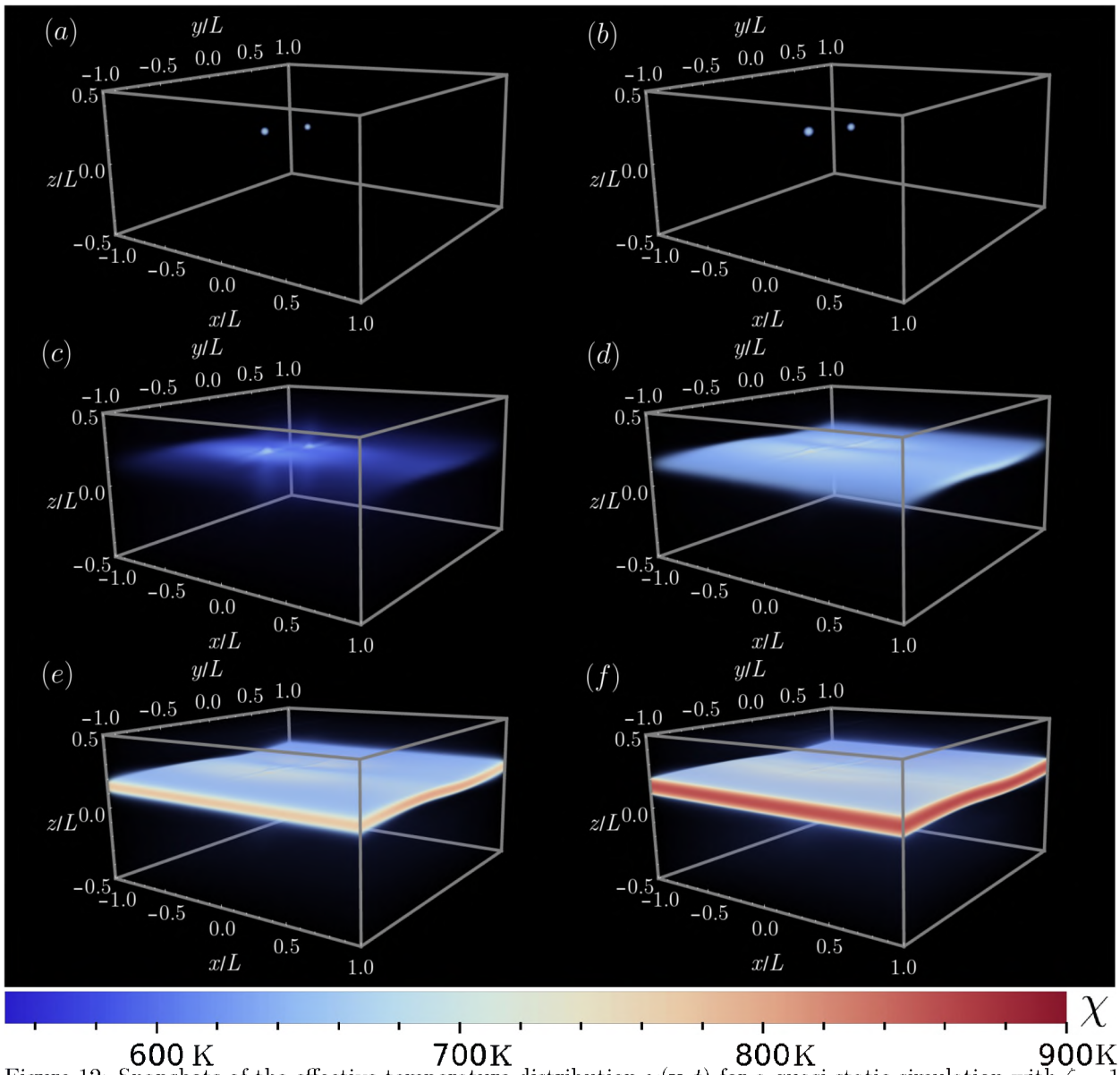

Figure 12: Snapshots of the effective temperature distribution $\chi(\mathbf{x}, t)$ for a quasi-static simulation with $\zeta = 1$. The initial condition is given in Eq. 40 with $\mathbf{X}_1 = (-0.5, -0.5, 0.35)$, $\mathbf{X}_2 = (-0.5, 0.5, 0.25)$. $a = 0.35$ and $\eta = 1.1$ for plots (a) (c). $a = 0.4$ and $\eta = 1.4$ for plots (d) (f). (a) $t = 0$. (b) $t = 10^5 t_s$. (c) $t = 2 \times 10^5 t_s$. (d) $t = 2.5 \times 10^5 t_s$. (e) $t = 3 \times 10^5 t_s$. (f) $t = 4 \times 10^5 t_s$.

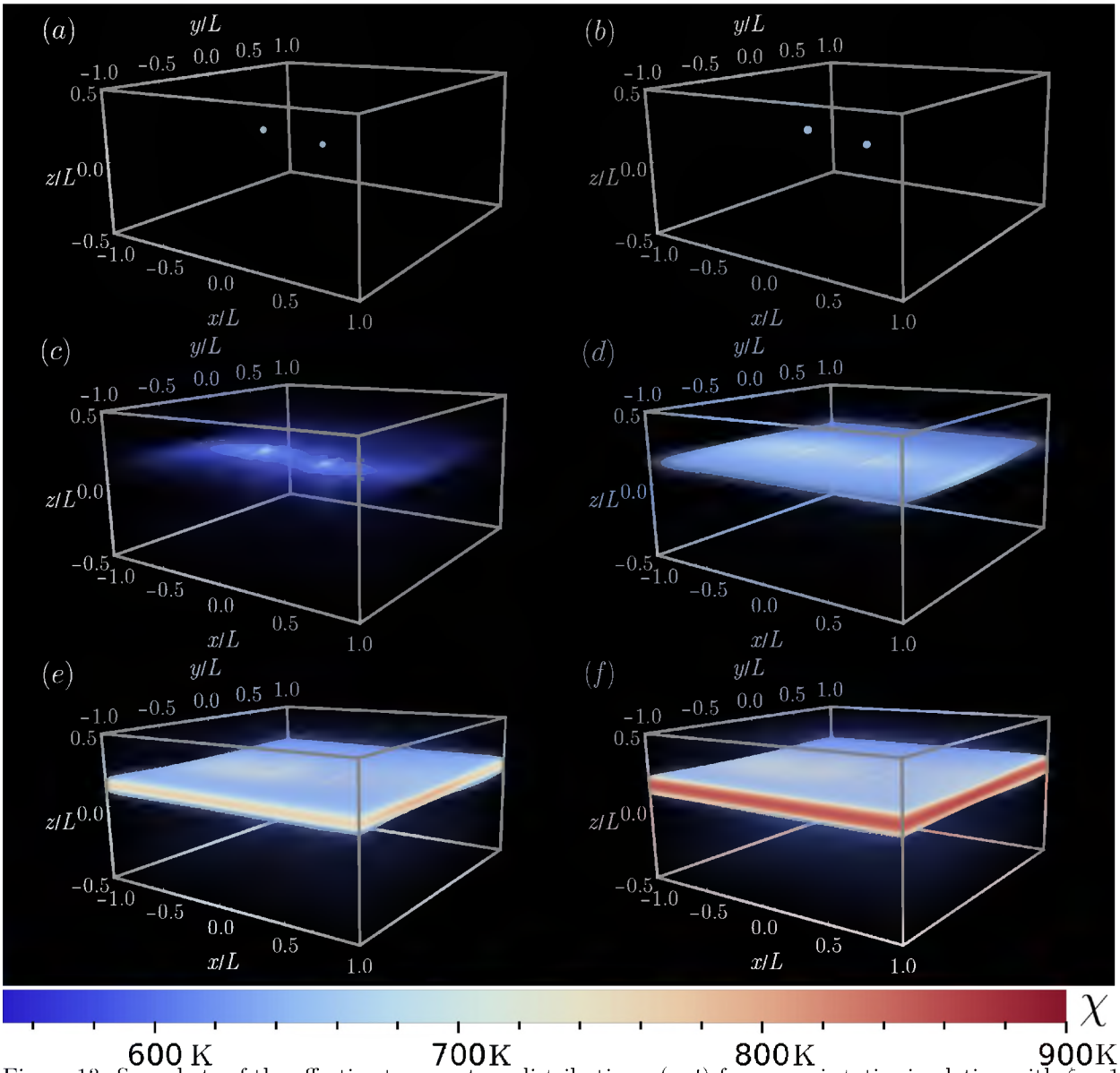

Figure 13: Snapshots of the effective temperature distribution $\chi(\mathbf{x}, t)$ for a quasi-static simulation with $\zeta = 1$. The initial condition is given in Eq. 40 with $\mathbf{X}_1 = (-0.5, -0.5, 0.35)$, $\mathbf{X}_2 = (0.5, -0.5, 0.25)$. $a = 0.35$ and $\eta = 1.1$ for plots (a) (c). $a = 0.4$ and $\eta = 1.4$ for plots (d) (f). (a) $t = 0$. (b) $t = 10^5 t_s$. (c) $t = 2 \times 10^5 t_s$. (d) $t = 2.5 \times 10^5 t_s$. (e) $t = 3 \times 10^5 t_s$. (f) $t = 4 \times 10^5 t_s$.

in Figs. 12(c) and 13(c) shows the initiation of shear band nucleation. In Fig. 12(d), we see the formation of a single curved band connecting the two defects, while in Fig. 13(d), the band is flat. Figs. 12(e), 12(f), 13(e), and 13(f) make this more clear as the band becomes more defined. The curvature seen in Fig. 12 is in the direction orthogonal to shear.

The dependence of band curvature on the relative orientation of the two defects can be best understood in terms of the qualitative structure of Fig. 11(c). There is a substantial extension of elevated χ along the x direction (parallel to shear, in-plane), a small extension along the y direction (orthogonal to shear, in-plane), and a moderate extension along the z direction (orthogonal to shear, out-of-plane). In Fig. 12, the defects are offset in y and z. Because the χ field is stronger in z than in y, this relative placement of the defects can accomodate curvature along the y direction. On the other hand, in Fig. 13, the defects are offset in x and z. The strength of the χ field extension in the x direction is great enough that the flat, horizontal regions of the two forming bands reach each other. The two bands join into one fatter flat band.

Taken together, Figs. 11, 12, & 13 provide insight into the structure and nucleation of shear bands from localized material defects. They help understand experimentally observed band curvature and raise the possibility that the placement and orientation of microscopic material properties can influence the qualitative structure of macroscopic shear bands. Finally, they provide intuition for more complex initial conditions, such as the random initializations considered later in this work, as a superposition of many defects.

4.3.1. Circular Defects

We now turn to a set of more complex initial conditions in the effective temperature field. Results for circular initial conditions parallel and perpendicular to the direction of shear are shown in Figs. 14 and 15 respectively. Mathematically, the initial conditions are

$$\begin{aligned} d &= \sqrt{\frac{y}{L} + \frac{z}{L}} - \frac{1}{4}, \\ \chi(\mathbf{x}, t = 0) &= 550 \text{ K} + (200 \text{ K}) \exp\left(-750 \left(d^2 + x^2\right)\right), \end{aligned} \tag{41}$$

and

$$\begin{aligned} d &= \sqrt{\frac{x}{L} + \frac{z}{L}} - \frac{1}{4}, \\ \chi(\mathbf{x}, t = 0) &= 550 \text{ K} + (200 \text{ K}) \exp\left(-750 \left(d^2 + y^2\right)\right), \end{aligned} \tag{42}$$

representing circles in the yz and xz planes respectively. Simulations were carried out using the same simulation geometry, discretization, quasi-static timestep, and boundary velocity as in the previous section. The initial conditions in Eqs. 41 and 42 are displayed in Figs. 14(a), 15(a) respectively.

By $t = 8 \times 10^4 t_s$ in Figs. 14(b) and 15(b) little has changed. At $t = 1.6 \times 10^5 t_s$ in Figs.14(c) and 15(c), differences due to the orientation of the circles become clear. The circle oriented perpendicular to shear closes vertically into a disk. The circle oriented along shear exhibits signatures of shear band nucleation at four equally space points. At $t = 2.5 \times 10^5 t_s$

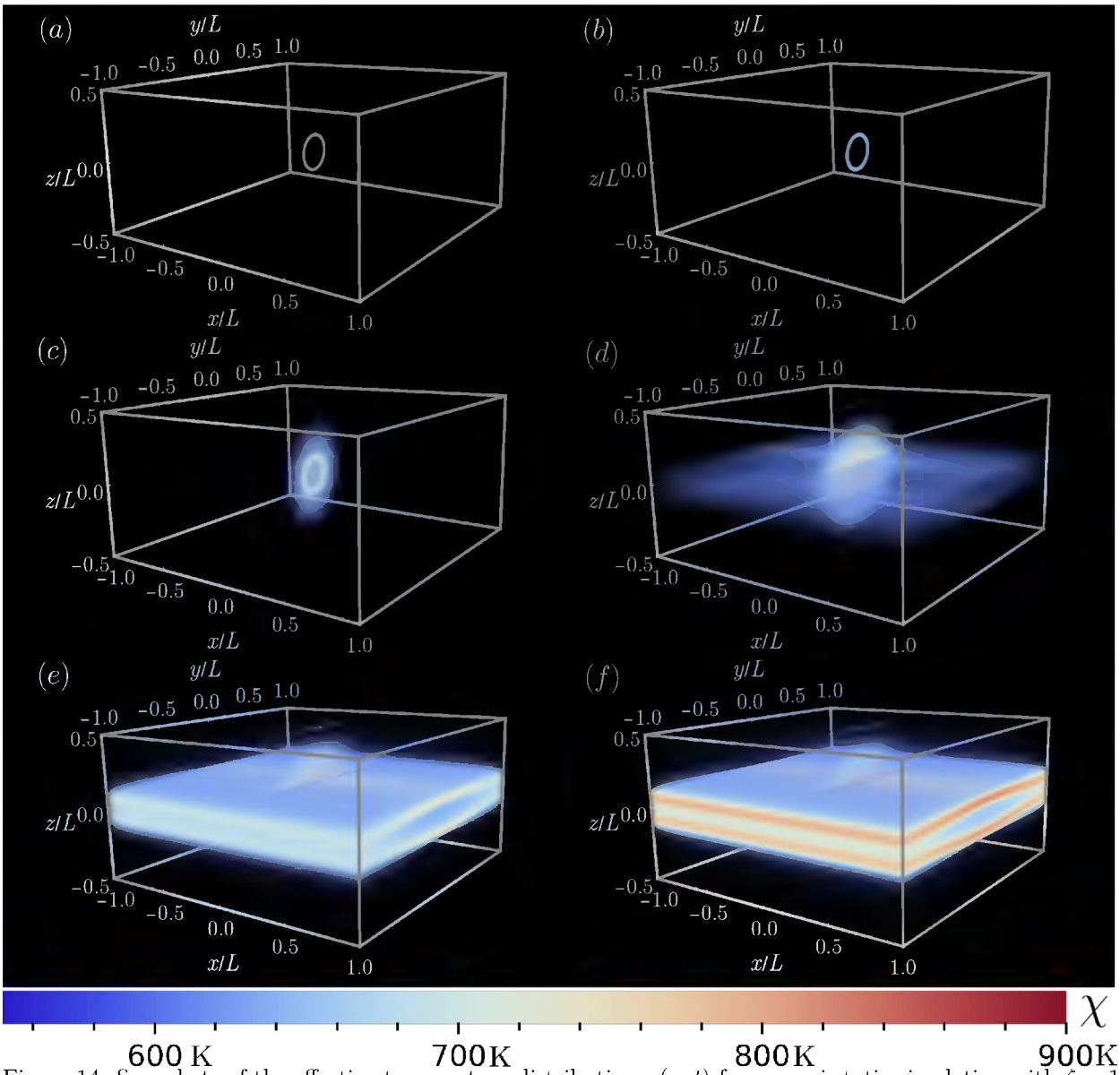

Figure 14: Snapshots of the effective temperature distribution $\chi(\mathbf{x}, t)$ for a quasi-static simulation with $\zeta = 1$. $a = 0.35$ and $\eta = 1.1$ in (a)–(c). $a = 0.4$ and $\eta = 1.4$ in (d)–(f). (a) $t = 0$ (b) $t = 8 \times 10^4 t_s$ (c) $t = 1.6 \times 10^5 t_s$ (d) $t = 2.4 \times 10^5 t_s$ (e) $t = 3.2 \times 10^5 t_s$ (f) $t = 4 \times 10^5 t_s$.

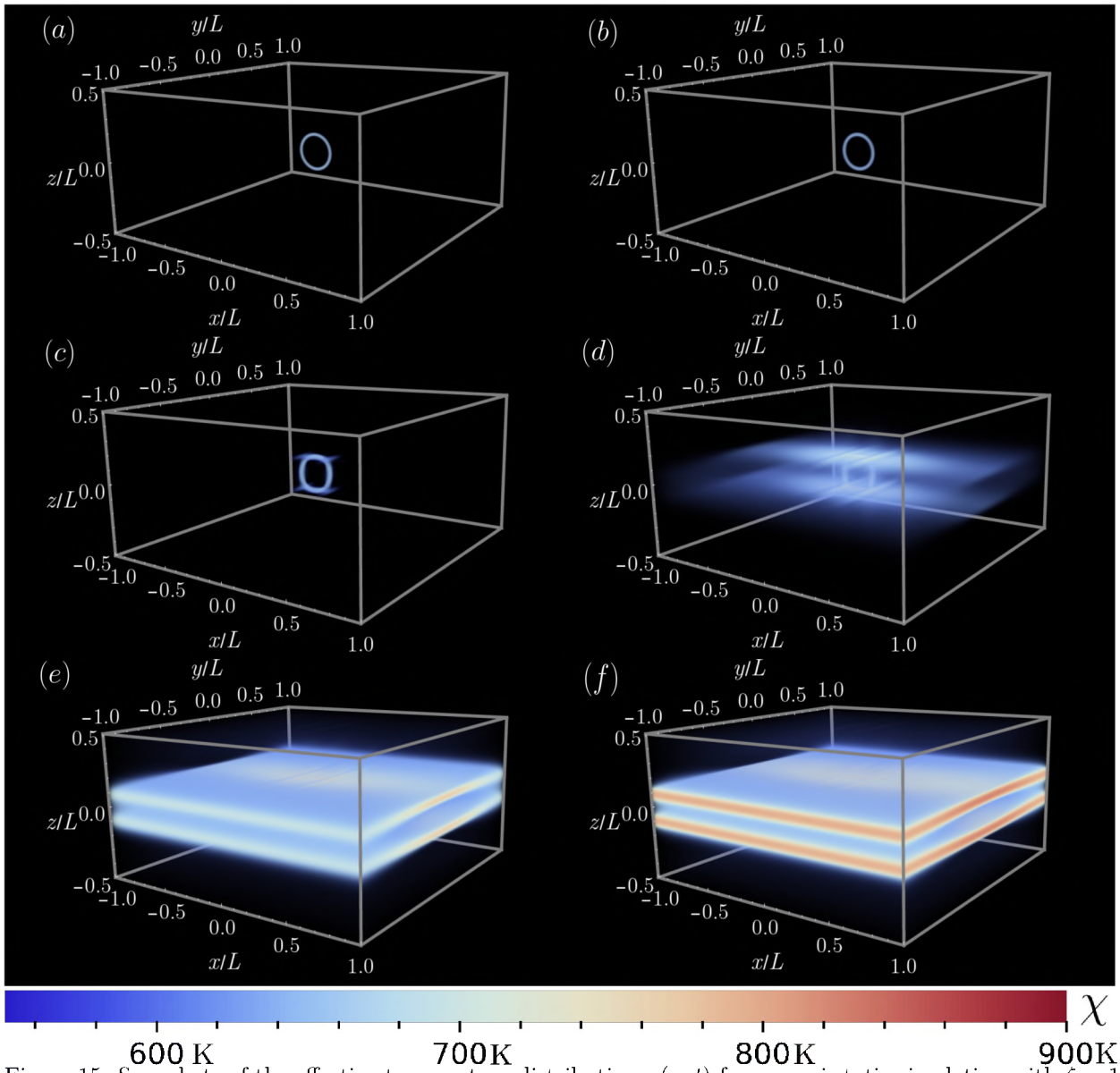

Figure 15: Snapshots of the effective temperature distribution $\chi(\mathbf{x}, t)$ for a quasi-static simulation with $\zeta = 1$. $a = 0.35$ and $\eta = 1.1$ in (a)–(c). $a = 0.4$ and $\eta = 1.4$ in (d)–(f). (a) $t = 0$ (b) $t = 8 \times 10^4 t_s$ (c) $t = 1.6 \times 10^5 t_s$ (d) $t = 2.4 \times 10^5 t_s$ (e) $t = 3.2 \times 10^5 t_s$ (f) $t = 4 \times 10^5 t_s$.

in Fig. 14(d), the disk has expanded and has developed a pointed front in the y direction. There are also two thick, curved bands forming close together near the center of the disk. In Fig. 15(d), there are two thinner, well-separated bands forming off the top and bottom of the circle with propagating fronts. By $t = 3.2 \times 10^5 t_s$ in Figs. 14(e) and 15(e), these differences have become even more prominent. The disk is still clear in Fig. 14(e) emerging from the two bands, and these bands are seen to have a curved structure in the y direction. They are also fatter and less separated than the bands seen in Fig. 15(e). These features continue to develop into the final pane at $t = 4 \times 10^5 t_s$. Taken together, Figs. 14 and 15 demonstrate another example of the dependence of shear banding structure and dynamics on the orientation of initial conditions in the χ field with respect to shear.

4.3.2. A randomly fluctuating effective temperature field

In this section, we consider the case of a randomly distributed initial effective temperature field. The initial conditions presented in the previous sections provide insight into the dynamics of shear banding, but it is unlikely that they have exact physical correspondences. The STZ theory postulates that STZs are randomly distributed throughout the material, and a random initial condition in χ is most faithful to this fundamental assumption [79]. Random initial conditions are thus expected to shed the most light on the structure of shear bands observed in experiments. The randomly fluctuating χ field furthermore leads to the formation of multiple shear bands, and potentially enables the study of shear band interactions in the STZ model [80].

We first populate the grid and a shell of ghost points with random variables $\chi_\zeta(\mathbf{x})$ using the Box–Muller algorithm. With μ_χ and σ_χ respectively denoting the desired mean and standard deviation, we perform the convolution

$$\chi(\mathbf{x}) = \frac{\sigma_\chi}{N} \sum_{\mathbf{r} \in V'} e^{-\frac{\|\mathbf{x}-\mathbf{r}\|^2}{l_c^2}} \chi_\zeta(\mathbf{r}) + \mu_\chi, \qquad N = \sqrt{\sum_{\mathbf{r} \in V} e^{-2\frac{\|\mathbf{r}\|^2}{l_c^2}}}. \tag{43}$$

where V denotes the set of grid points and V' denotes the set of grid points with the addition of the ghost points. Equation 43 ensures that the effective temperature value at each point is normally distributed with mean μ_χ and standard deviation σ_χ. In practice, the sums in Eq. 43 are performed with a cutoff length scale specified as a multiplicative factor of the convolution length scale l_c, and the number of ghost points in V' is set by the choice of cutoff length scale. Results for a random initialization with $\mu_\chi = 500$ K, $\sigma_\chi = 15$ K, $l_c = 5h$ and a cutoff factor of 5 (leaded to 25 ghost points in each direction for the convolution) are shown in Fig. 16. The grid is of size $512 \times 512 \times 256$. The simulation geometry, quasi-static timestep, and boundary velocity are the same as in previous sections. The initial conditions are shown in Fig. 16(a).

By $t = 5 \times 10^4 t_s$ in Fig. 16(b), the effective temperature has increased somewhat uniformly across the grid. At $t = 10^5 t_s$ in Fig. 16(c), both horizontal and vertical shear bands begin to nucleate throughout the simulation. Fig. 16(d) displays a multitude of thin, system-spanning horizontal bands connected by vertical bands. Curvature is present in the horizontal bands both parallel and orthogonal to the direction of shear. A branching pattern is seen at

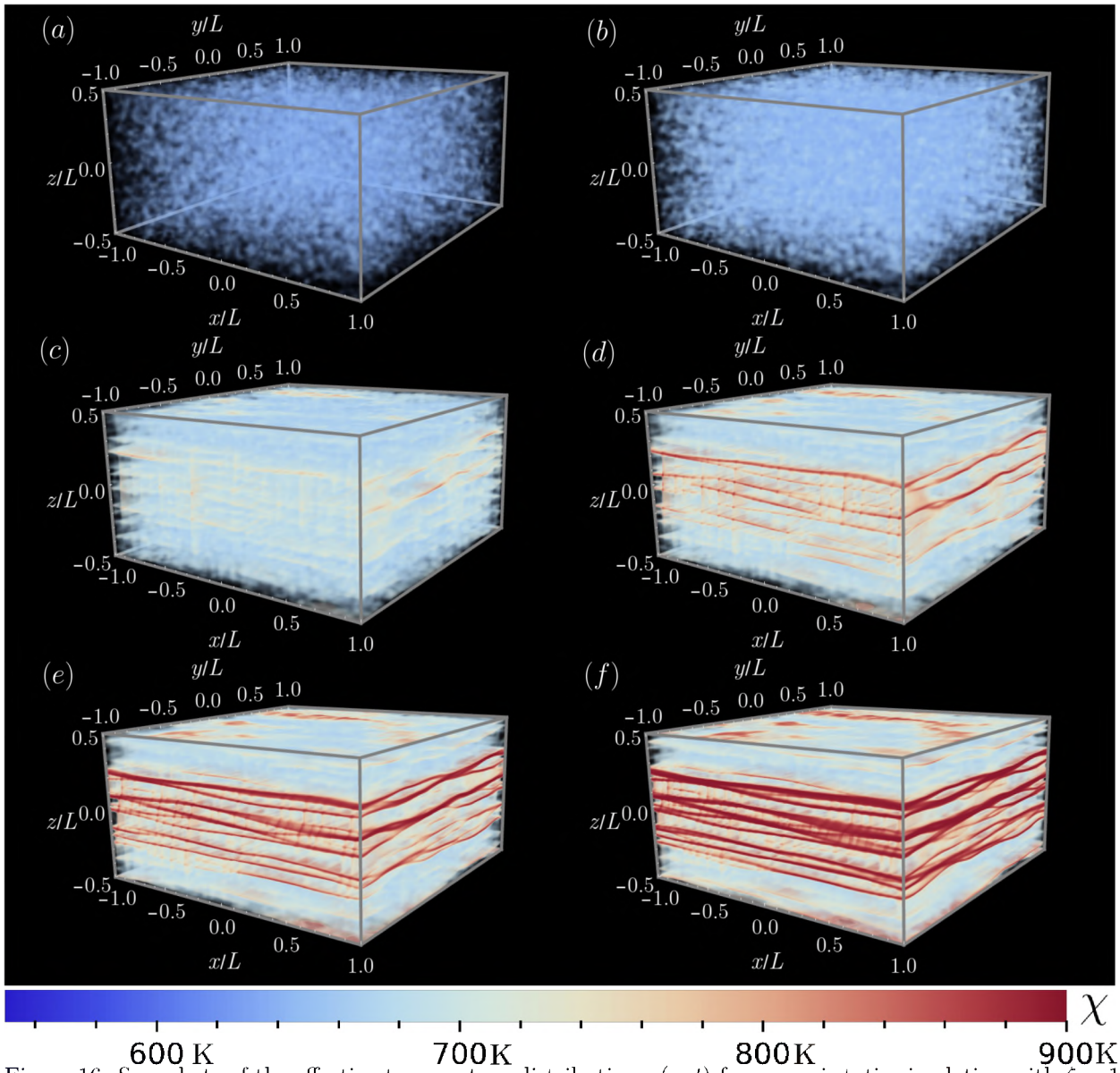

Figure 16: Snapshots of the effective temperature distribution $\chi(\mathbf{x}, t)$ for a quasi-static simulation with $\zeta = 1$. $a = 0.6$ and $\eta = 1.5$ for subfigures (a) and (b). $a = 0.7$ and $\eta = 1.55$ for subfigures (c)–(**f**). (a) $t = 0$. (b) $t = 5 \times 10^4 t_s$. (c) $t = 10^5 t_s$. (d) $t = 1.5 \times 10^5 t_s$. (e) $t = 2.5 \times 10^5 t_s$. (f) $t = 4 \times 10^5 t_s$.

$t = 2.5 \times 10^5 t_s$ and $t = 4 \times 10^5 t_s$ in Figs. 16(e) and (f), where thick bands split into two thinner bands and later rejoin.

5. Interim Remarks

We have discussed a family of quasi-static projection methods for hypo-elastoplasticity through an analogy with incompressible fluid dynamics. A single member of this family was chosen, and a discrete scheme was developed for use in three dimensions, generalizing previous work in two dimensions [23]. Several numerical examples were considered within the shear transformation zone model of amorphous plasticity, and both qualitative and quantitative convergence of the quasi-static method to an explicit scheme was demonstrated.

In part II of this paper [63], the hypo-elastoplastic equations are derived in a fixed reference domain that can be related to a physically deforming grid through a time-dependent linear transformations $\mathbf{T}(t)$. This framework enables straightforward implementation of several otherwise complex continuum-scale boundary conditions, such as pure shear and the Lees–Edwards boundary conditions used in molecular dynamics simulations. The projection method developed is extended to the transformed domain. We demonstrate the convergence of the transformed method to the standard method presented here in a physically equivalent setup. Several other interesting numerical examples within the shear transformation zone model of amorphous plasticity are considered, including the dependence of shear banding dynamics with random initializations in χ on the mean μ_χ of the distribution. Particular attention is paid to the effect of periodicity in z on shear banding dynamics. Part two concludes with a summary of the ideas discussed here and in part II itself.

Appendix A. Connection to the continuous-time framework

We can make a connection to the general continuous-time framework presented in Sec. 2.4 as follows. By comparison of Eqs. 16 and 28, we can identify $\mathbf{\Phi} = \Delta t\ \mathbf{v}$. Equation 15 then says that

$$\mathbf{C} : \mathbf{D}^{n+1} = \mathbf{C} : \left(\nabla \mathbf{q} + \Delta t \frac{\partial \mathbf{D}^{n+1}}{\partial t} \right). \tag{A.1}$$

Recall that $\mathbf{q}$ is chosen to be the best available approximation to $\mathbf{v}^{n+1}$, and note that by symmetry of $\mathbf{C}$,

$$\mathbf{C} : \nabla q = \mathbf{C} : \frac{1}{2} \left(\nabla \mathbf{q} + \nabla \left(\mathbf{q} \right)^{\mathsf{T}} \right). \tag{A.2}$$

Equation A.1 thus says the following: $\mathbf{C} : \mathbf{D}^{n+1}$ is given by the best available guess before the solve for $\mathbf{v}^{n+1}$ - $\mathbf{C} : \nabla \mathbf{q}$ - plus an $\mathcal{O}(\Delta t)$ correction constructed via a first-order Taylor expansion in time.

Acknowledgments

The authors thank Eran Bouchbinder and Avraham Moriel (Weizmann Institute of Science) for useful discussions about this work. This work was supported by the National Science

Foundation under Grant Nos. DMR-1409560 and DMS-1753203. N. M. Boffi was supported by a Department of Energy Computational Science Graduate Fellowship. C. H. Rycroft was partially supported by the Applied Mathematics Program of the U.S. DOE Office of Advanced Scientific Computing Research under contract number DE-AC02-05CH11231.

References

[1] J. Ju, L. Sun, *Effective elastoplastic behavior of metal matrix composites containing randomly located aligned spheroidal inhomogeneities. Part I: micromechanics-based formulation*, International Journal of Solids and Structures **38** (2001) 183–201. doi:10.1016/S0020-7683(00)00023-8.

[2] J. Dirrenberger, S. Forest, D. Jeulin, *Elastoplasticity of auxetic materials*, Computational Materials Science **64** (2012) 57–61, proceedings of the 21st International Workshop on Computational Mechanics of Materials (IWCMM 21). doi:10.1016/j.commatsci.2012.03.036.

[3] A. Daouadji, P.-Y. Hicher, A. Rahma, *An elastoplastic model for granular materials taking into account grain breakage*, European Journal of Mechanics - A/Solids **20** (2001) 113–137. doi:10.1016/S0997-7538(00)01130-X.

[4] M. Moner-Girona, A. Roig, E. Molins, E. Martínez, J. Esteve, *Micromechanical properties of silica aerogels*, Applied Physics Letters **75** (1999) 653–655. doi:10.1063/1.124471.

[5] A. Gouldstone, H.-J. Koh, K.-Y. Zeng, A. Giannakopoulos, S. Suresh, *Discrete and continuous deformation during nanoindentation of thin films*, Acta Materialia **48** (2000) 2277–2295. doi:10.1016/S1359-6454(00)00009-4.

[6] J. Schroers, *Bulk Metallic Glasses*, Physics Today **66** (2013) 32–37. doi:10.1063/PT.3.1885.

[7] H. Xiao, O. Bruhns, A. Meyers, *Elastoplasticity beyond small deformations*, Acta Mechanica **182** (2006) 31–111. doi:10.1007/s00707-005-0282-7.

[8] M. E. Gurtin, E. Fried, L. Anand, The Mechanics and Thermodynamics of Continua, Cambridge University Press, Cambridge, 2010.

[9] W. Prager, *An elementary discussion of definitions of stress rate*, Quart. Appl. Math. **18** (1960) 403–407.

[10] E. Kröner, *Allgemeine Kontinuumstheorie der Versetzungen und Eigenspannungen*, Archive for Rational Mechanics and Analysis **4** (1959) 273–334. doi:10.1007/BF00281393.

[11] E. H. Lee, *Elastic–Plastic Deformation at Finite Strains*, Journal of Applied Mechanics **36** (1969) 1–6. doi:10.1115/1.3564580.

[12] C. Truesdell, *Hypo-Elasticity*, Indiana Univ. Math. J. **4** (1955) 83–133.

[13] R. Hill, *A general theory of uniqueness and stability in elastic–plastic solids*, Journal of the Mechanics and Physics of Solids **6** (1958) 236–249. doi:10.1016/0022-5096(58)90029-2.

[14] J. B. Bell, P. Colella, H. M. Glaz, *A second-order projection method for the incompressible Navier–Stokes equations*, Journal of Computational Physics **85** (1989) 257–283. doi:10.1016/0021-9991(89)90151-4.

[15] A. Almgren, J. Bell, W. Szymczak, *A Numerical Method for the Incompressible Navier–Stokes Equations Based on an Approximate Projection*, SIAM Journal on Scientific Computing **17** (1996) 358–369. doi:10.1137/S1064827593244213.

[16] J.-D. Yu, S. Sakai, J. A. Sethian, *A coupled level set projection method applied to ink jet simulation*, Interfaces and Free Boundaries **5** (2003) 459–482.

[17] C. S. Peskin, *The immersed boundary method*, Acta Numerica **11** (2002) 479–517. doi:10.1017/S0962492902000077.

[18] B. E. Griffith, X. Luo, D. M. McQueen, C. S. Peskin, *Simulating the fluid dynamics of natural and prosthetic heat valves using the immersed boundary method*, Int. J. Appl. Mech. **1** (2009) 137–177. doi:10.1142/S1758825109000113.

[19] T. G. Fai, C. H. Rycroft, *Lubricated immersed boundary method in two dimensions*, Journal of Computational Physics **356** (2018) 319–339. doi:10.1016/j.jcp.2017.11.029.

[20] W. L. Briggs, V. E. Henson, S. F. McCormick, A Multigrid Tutorial: Second Edition, Society for Industrial and Applied Mathematics, Philadelphia, PA, USA, 2000.

[21] J. W. Demmel, Applied Numerical Linear Algebra, SIAM, 1997.

[22] R. Courant, K. Friedrichs, H. Lewy, *On the Partial Difference Equations of Mathematical Physics*, IBM Journal of Research and Development **11** (1967) 215–234. doi:10.1147/rd.112.0215.

[23] C. H. Rycroft, Y. Sui, E. Bouchbinder, *An Eulerian projection method for quasi-static elastoplasticity*, Journal of Computational Physics **300** (2015) 136–166. doi:10.1016/j.jcp.2015.06.046.

[24] A. J. Chorin, *A numerical method for solving incompressible viscous flow problems*, Journal of Computational Physics **2** (1967) 12–26. doi:10.1016/0021-9991(67)90037-X.

[25] A. J. Chorin, *Numerical Solution of the Navier–Stokes Equations*, Mathematics of Computation **22** (1968) 745–762. doi:10.1090/S0025-5718-1968-0242392-2.

[26] M. L. Falk, J. S. Langer, *Dynamics of viscoplastic deformation in amorphous solids*, Phys. Rev. E **57** (1998) 7192–7205. doi:10.1103/PhysRevE.57.7192.

[27] E. Bouchbinder, J. S. Langer, I. Procaccia, *Athermal shear-transformation-zone theory of amorphous plastic deformation. I. Basic principles*, Phys. Rev. E **75** (2007) 036107. doi:10.1103/PhysRevE.75.036107.

[28] J. S. Langer, *Shear-transformation-zone theory of plastic deformation near the glass transition*, Phys. Rev. E **77** (2008) 021502. doi:10.1103/PhysRevE.77.021502.

[29] E. Bouchbinder, J. S. Langer, *Nonequilibrium thermodynamics of driven amorphous materials. I. Internal degrees of freedom and volume deformation*, Phys. Rev. E **80** (2009) 031131. doi:10.1103/PhysRevE.80.031131.

[30] J. J. Kruzic, *Bulk Metallic Glasses as Structural Materials: A Review*, Advanced Engineering Materials **18** (2016) 1308–1331. doi:10.1002/adem.201600066.

[31] T. C. Hufnagel, T. Jiao, Y. Li, L.-Q. Xing, K. T. Ramesh, *Deformation and Failure of Zr57Ti5Cu20Ni8Al10 Bulk Metallic Glass Under Quasi-static and Dynamic Compression*, Journal of Materials Research **17** (2002) 1441–1445. doi:10.1557/JMR.2002.0214.

[32] M. L. Manning, J. S. Langer, J. M. Carlson, *Strain localization in a shear transformation zone model for amorphous solids*, Phys. Rev. E **76** (2007) 056106. doi:10.1103/PhysRevE.76.056106.

[33] M. L. Manning, E. G. Daub, J. S. Langer, J. M. Carlson, *Rate-dependent shear bands in a shear-transformation-zone model of amorphous solids*, Phys. Rev. E **79** (2009) 016110. doi:10.1103/PhysRevE.79.016110.

[34] B. A. Sun, S. Pauly, J. Hu, W. H. Wang, U. Kühn, J. Eckert, *Origin of Intermittent Plastic Flow and Instability of Shear Band Sliding in Bulk Metallic Glasses*, Phys. Rev. Lett. **110** (2013) 225501. doi:10.1103/PhysRevLett.110.225501.

[35] J. Antonaglia, W. J. Wright, X. Gu, R. R. Byer, T. C. Hufnagel, M. LeBlanc, J. T. Uhl, K. A. Dahmen, *Bulk Metallic Glasses Deform via Slip Avalanches*, Phys. Rev. Lett. **112** (2014) 155501. doi:10.1103/PhysRevLett.112.155501.

[36] L. O. Eastgate, J. S. Langer, L. Pechenik, *Dynamics of Large-Scale Plastic Deformation and the Necking Instability in Amorphous Solids*, Phys. Rev. Lett. **90** (2003) 045506. doi:10.1103/PhysRevLett.90.045506.

[37] C. H. Rycroft, F. Gibou, *Simulations of a stretching bar using a plasticity model from the shear transformation zone theory*, Journal of Computational Physics **231** (2012) 2155–2179. doi:10.1016/j.jcp.2011.10.009.

[38] A. Moriel, E. Bouchbinder, *Necking instabilities in elastoviscoplastic materials*, Phys. Rev. Materials **2** (2018) 073602. doi:10.1103/PhysRevMaterials.2.073602.

[39] C. H. Rycroft, E. Bouchbinder, *Fracture Toughness of Metallic Glasses: Annealing-induced embrittlement*, Phys. Rev. Lett. **109** (2012) 194301. doi:10.1103/PhysRevLett.109.194301.

[40] M. Vasoya, C. H. Rycroft, E. Bouchbinder, *Notch Fracture Toughness of Glasses: Dependence on Rate, Age, and Geometry*, Phys. Rev. Applied **6** (2016) 024008. doi:10.1103/PhysRevApplied.6.024008.

[41] J. Ketkaew, W. Chen, H. Wang, A. Datye, M. Fan, G. Pereira, U. D. Schwarz, Z. Liu, R. Yamada, W. Dmowski, M. D. Shattuck, C. S. O'Hern, T. Egami, E. Bouchbinder, J. Schroers, *Mechanical glass transition revealed by the fracture toughness of metallic glasses*, Nature Communications **9** (2018) 3271. doi:10.1038/s41467-018-05682-8. URL https://doi.org/10.1038/s41467-018-05682-8

[42] A. Greer, Y. Cheng, E. Ma, *Shear bands in metallic glasses*, Materials Science and Engineering: R: Reports **74** (2013) 71–132. doi:10.1016/j.mser.2013.04.001.

[43] R. Maa, J. F. Lffler, *Shear-Band Dynamics in Metallic Glasses*, Advanced Functional Materials **25** (2015) 2353–2368. doi:10.1002/adfm.201404223.

[44] Y. Zhang, A. L. Greer, *Thickness of shear bands in metallic glasses*, Applied Physics Letters **89** (2006) 071907. doi:10.1063/1.2336598.

[45] B. Yang, M. L. Morrison, P. K. Liaw, R. A. Buchanan, G. Wang, C. T. Liu, M. Denda, *Dynamic evolution of nanoscale shear bands in a bulk-metallic glass*, Applied Physics Letters **86** (2005) 141904. doi:10.1063/1.1891302.

[46] C. A. Schuh, T. C. Hufnagel, U. Ramamurty, *Mechanical behavior of amorphous alloys*, Acta Materialia **55** (2007) 4067–4109. doi:10.1016/j.actamat.2007.01.052.

[47] R. Maa, K. Samwer, W. Arnold, C. A. Volkert, *A single shear band in a metallic glass: Local core and wide soft zone*, Applied Physics Letters **105** (2014) 171902. doi:10.1063/1.4900791.

[48] A. S. Argon, *Plastic deformation in metallic glasses*, Acta Metallurgica **27** (1979) 47–58.

[49] H. Xiao, O. T. Bruhns, A. Meyers, *Hypo-Elasticity Model Based upon the Logarithmic Stress Rate*, Journal of Elasticity **47** (1997) 51–68. doi:10.1023/A:1007356925912.

[50] C. Truesdell, *HypoElastic Shear*, Journal of Applied Physics **27** (1956) 441–447. doi:10.1063/1.1722399.

[51] J. Bardet, *Finite element analysis of surface instability in hypo-elastic solids*, Computer Methods in Applied Mechanics and Engineering **78** (1990) 273–296. doi:10.1016/0045-7825(90)90002-4.

[52] S. Hajarolasvadi, A. E. Elbanna, *A new hybrid numerical scheme for modelling elastodynamics in unbounded media with near-source heterogeneities*, Geophysical Journal International **211** (2017) 851–864. doi:10.1093/gji/ggx337.

[53] X. Ma, A. Elbanna, *Strain localization in dry sheared granular materials: A compactivity-based approach*, Phys. Rev. E **98** (2018) 022906. doi:10.1103/PhysRevE.98.022906.

[54] T. J. Hughes, Numerical Implementation of Constitutive Models: Rate-Independent Deviatoric Plasticity, Springer, 1984.

[55] L. Anand, M. Kothari, *A computational procedure for rate-independent crystal plasticity*, Journal of the Mechanics and Physics of Solids **44** (1996) 525–558. doi:10.1016/0022-5096(96)00001-4.

[56] G. Puglisi, L. Truskinovsky, *Thermodynamics of rate-independent plasticity*, Journal of the Mechanics and Physics of Solids **53** (2005) 655–679. doi:10.1016/j.jmps.2004.08.004.

[57] J. Simo, R. Taylor, *Consistent tangent operators for rate-independent elastoplasticity*, Computer Methods in Applied Mechanics and Engineering **48** (1985) 101–118. doi:10.1016/0045-7825(85)90070-2.

[58] R. Saye, *Implicit mesh discontinuous Galerkin methods and interfacial gauge methods for high-order accurate interface dynamics, with applications to surface tension dynamics, rigid body fluidstructure interaction, and free surface flow: Part I*, Journal of Computational Physics **344** (2017) 647–682. doi:10.1016/j.jcp.2017.04.076.

[59] R. Saye, *Implicit mesh discontinuous Galerkin methods and interfacial gauge methods for high-order accurate interface dynamics, with applications to surface tension dynamics, rigid body fluidstructure interaction, and free surface flow: Part II*, Journal of Computational Physics **344** (2017) 683–723. doi:10.1016/j.jcp.2017.05.003.

[60] R. Saye, *Interfacial gauge methods for incompressible fluid dynamics*, Science Advances **2**. doi:10.1126/sciadv.1501869.

[61] D. L. Brown, R. Cortez, M. L. Minion, *Accurate Projection Methods for the Incompressible Navier–Stokes Equations*, J. Comput. Phys. **168** (2001) 464–499. doi:10.1006/jcph.2001.6715.

[62] C. Min, F. Gibou, *A second order accurate projection method for the incompressible Navier–Stokes equations on non-graded adaptive grids*, Journal of Computational Physics **219** (2006) 912–929. doi:10.1016/j.jcp.2006.07.019.

[63] N. M. Boffi, C. H. Rycroft, *Parallel three-dimensional simulations of quasi-static elastoplastic solids. Part II: Coordinate transformations*, arXiv e-prints.

[64] J. Lubliner, Plasticity Theory, Dover, New York, 2008.

[65] K. Kamrin, E. Bouchbinder, *Two-temperature continuum thermomechanics of deforming amorphous solids*, Journal of the Mechanics and Physics of Solids **73** (2014) 269–288. doi:10.1016/j.jmps.2014.09.009.

[66] E. Bouchbinder, J. S. Langer, *Shear-transformation-zone theory of linear glassy dynamics*, Phys. Rev. E **83** (2011) 061503. doi:10.1103/PhysRevE.83.061503.

[67] E. Bouchbinder, *Effective temperature dynamics in an athermal amorphous plasticity theory*, Phys. Rev. E **77** (2008) 051505.

[68] D. Loi, S. Mossa, L. F. Cugliandolo, *Effective temperature of active matter*, Phys. Rev. E **77** (2008) 051111. doi:10.1103/PhysRevE.77.051111.

[69] L. F. Cugliandolo, *The effective temperature*, Journal of Physics A: Mathematical and Theoretical **44** (2011) 483001.

[70] M. L. Falk, J. Langer, *Deformation and Failure of Amorphous, Solidlike Materials*, Annual Review of Condensed Matter Physics **2** (2011) 353–373. doi:10.1146/annurev-conmatphys-062910-140452.

[71] E. Bouchbinder, J. S. Langer, I. Procaccia, *Athermal shear-transformation-zone theory of amorphous plastic deformation. II.Analysis of simulated amorphous silicon*, Phys. Rev. E **75** (2007) 036108. doi:10.1103/PhysRevE.75.036108.

[72] M. T. Heath, Scientific Computing: An Introductory Survey, McGraw-Hill, 2002.

[73] C.-W. Shu, S. Osher, *Efficient implementation of essentially non-oscillatory shock-capturing schemes*, J. Comp. Phys. **77** (1988) 439–471. doi:10.1016/0021-9991(88)90177-5.

[74] E. Gabriel, G. E. Fagg, G. Bosilca, T. Angskun, J. J. Dongarra, J. M. Squyres, V. Sahay, P. Kambadur, B. Barrett, A. Lumsdaine, R. H. Castain, D. J. Daniel, R. L. Graham, T. S. Woodall, *Open MPI: Goals, Concept, and Design of a Next Generation MPI Implementation*, in: Proceedings, 11th European PVM/MPI Users' Group Meeting, Budapest, Hungary, 2004, pp. 97–104.

[75] W. L. Briggs, V. E. Henson, S. F. McCormick, A Multigrid Tutorial, SIAM, 2000.

[76] J. Xu, *Iterative Methods by Space Decomposition and Subspace Correction*, SIAM Review **34** (1992) 581–613. doi:10.1137/1034116.

[77] M. Theillard, C. H. Rycroft, F. Gibou, *A Multigrid Method on Non-Graded Adaptive Octree and Quadtree Cartesian Grids*, Journal of Scientific Computing **55** (2013) 1–15. doi:10.1007/s10915-012-9619-2.

[78] J. Li, Z. L. Wang, T. C. Hufnagel, *Characterization of nanometer-scale defects in metallic glasses by quantitative high-resolution transmission electron microscopy*, Phys. Rev. B **65** (2002) 144201. doi:10.1103/PhysRevB.65.144201.

[79] A. R. Hinkle, C. H. Rycroft, M. D. Shield, M. L. Falk, *Coarse graining atomistic simulations of plastically deforming amorphous solids*, Phys. Rev. E **95** (2017) 053001. doi:10.1103/PhysRevE.95.053001.

[80] B. Sun, S. Pauly, J. Tan, M. Stoica, W. Wang, U. Khn, J. Eckert, *Serrated flow and stickslip deformation dynamics in the presence of shear-band interactions for a Zr-based metallic glass*, Acta Materialia **60** (2012) 4160–4171. doi:10.1016/j.actamat.2012.04.013.